Radiative forcing of anthropogenic aerosols on cirrus clouds using a hybrid ice nucleation scheme

Jialei Zhu[1,2] and Joyce E. Penner[2]

1 Institute of Surface-Earth System Science, Tianjin University, Tianjin 300072, China

2 Department of Climate and Space Sciences and Engineering, University of Michigan, Ann Arbor, Michigan 48109, USA

Corresponding Author: Jialei Zhu (Email: zhujialei@tju.edu.cn)

Abstract

Anthropogenic aerosols impact cirrus clouds through ice nucleation, thereby changing the Earth's radiation budget. However, the magnitude and sign of anthropogenic forcing in cirrus clouds is still very uncertain depending on the treatments for ice nucleating particles (INPs), for haze particle freezing, and the ice nucleation scheme. In this study, a new ice nucleation scheme (hereafter the HYBRID scheme) is developed to combine the best features of two previous ice nucleation schemes, so that global models are able to calculate the ice number concentration in both updrafts and downdrafts associated with gravity waves and has a robust sensitivity to the change of aerosol number. The scheme is applied in a box model, and the ice number concentrations (9.52±2.08 L^{-1}) are somewhat overestimated but are in reasonable agreement with those from an adiabatic parcel model (9.40±2.31 L^{-1}). Then, the forcing and cloud changes associated with changes in aircraft soot, sulfur emission and all anthropogenic emissions between the preindustrial (PI) period and the present day (PD) are examined using the

CESM/IMPACT global model with the HYBRID scheme. Aircraft soot emissions decrease the global average ice number concentration (Ni) by -1.0±2.4×10^7 m^{-2} (-1%) (over the entire column) due to the inhibition of homogeneous nucleation and lead to a radiative forcing of -0.14±0.07 W m^{-2}, while the increase in sulfur emissions increases the global average Ni by 7.3±2.9×10^7 m^{-2} (5%) due to the increase in homogeneous nucleation and leads to a radiative forcing of -0.02±0.06 W m^{-2}. The possible effects of aerosol and cloud feedbacks to the meteorological state in remote regions partly contribute to reduce the forcing and the change in Ni due to anthropogenic emissions. The radiative forcing due to all increased anthropogenic emissions from PI to PD is estimated to be -0.20±0.05 W m^{-2}. If newly formed secondary organic aerosols (SOA) act an INPs and inhibit homogeneous nucleation, the Ni formed from heterogeneous nucleation is increased. As a result, the inclusion of INPs from SOA increases the change in Ni to 12.0±2.3×10^7 m^{-2} (9%) and increases (makes less negative) the anthropogenic forcing on cirrus clouds to -0.04±0.08 W m^{-2} from PI to PD.

1. Introduction

Atmospheric aerosol loading has increased significantly since the PI period, mainly due to anthropogenic emissions associated with the burning of fossil fuels and biomass. Most studies to date have focused on how the increase in anthropogenic aerosols impacts climate via warm clouds thereby exerting a net cooling effect (Wang and Penner, 2009; Zhu et al., 2019; Gordon et al., 2016; IPCC, 2013). Compared to warm clouds, there has been much less attention paid to anthropogenic forcing as a result of changes to cirrus clouds, which is one of the least understood processes in the climate system (Fan et al., 2016). Cirrus clouds cover about 30% of the Earth's area (Wang et al., 1996) and play an important role in the Earth's

radiation budget and also influence global precipitation and the hydrologic cycle (Waliser et al., 2009; Hong et al., 2016; Matus, A. V. and L'Ecuyer 2017). Ice particles in cirrus clouds are nucleated on aerosol particles, so that changes to the aerosol composition and loading may alter cirrus clouds by altering cloud microphysics, resulting in a cirrus cloud radiative forcing.

There are major uncertainties in calculating the radiative forcing of cirrus clouds using global climate models, both in terms of its magnitude (since PI) and its sign (Storelvmo, 2017). The ice particles in the cirrus clouds can form either by homogeneous freezing of solution droplets (or haze particles) (Koop et al., 2000) or by heterogeneous nucleation of INPs (Cantrell and Heymsfield, 2005). Supercooled aqueous solutions such as sulfate haze particles can form ice through homogeneous nucleation when the relative humidity with respect to ice (RHi) is high (of order 150%), which may be the dominant mechanism for the ice formation in cirrus clouds (Hendricks et al., 2011; Penner et al., 2018). However, heterogeneous ice nucleation of INPs formed from dust, soot and other insoluble aerosols requires much lower RHi, so that heterogeneous nucleation is able to occur in advance of homogeneous nucleation in a rising air parcel (Hoose and Möhler, 2012). As a result, heterogeneous and homogeneous ice formation compete for the available water vapor. Heterogeneous nucleation can lead to a significant reduction of the number of ice particles that form compared to homogeneous freezing because the number of INPs is much smaller than the number of haze particles. However, if additional INPs are added to a region where heterogeneous nucleation already dominates, an increase in ice crystal number is expected. Therefore, the radiative effect of aerosols on cirrus clouds could differ in both magnitude and sign depending on the competition between these two ice nucleation processes. Ice nucleation by INPs vs haze freezing

is determined by both the number of homogeneous and heterogeneous ice nucleating particles as well as the updraft velocity or cooling rate.

Despite the relatively low level of understanding of ice nucleation, a few physically based parameterizations that treat the competition between homogeneous and heterogeneous nucleation have been developed in order to study the effect of ice nucleation in global climate models (Liu and Penner, 2005; Kärcher et al., 2006; Barahona and Nenes, 2008). The Liu and Penner (2005) parameterization (hereafter LP) is derived from fitting the simulation results of an adiabatically rising cloud parcel (Liu and Penner, 2005). The LP parameterization is only able to treat cases for which the updraft velocity is positive, so the evaporation of drops during downdrafts is neglected. The parameterization developed by Barahona and Nenes (2008) (hereafter BN) is derived from an analytical solution of the cloud parcel equations (Barahona and Nenes, 2008). The LP and BN parameterizations always show a similar trend when there is an increase in either the haze aerosol number concentrations or INPs, (Shi and Liu, 2018) and they result in very similar ice number concentrations when the water vapor accommodation coefficient is set to 0.1 (Zhou et al., 2016). The Kärcher et al. (2006) parameterization (hereafter KL) explicitly calculates the evolution of ice supersaturation in a rising cloud parcel when different aerosol types freeze (Kärcher et al., 2006). The KL parameterization was used in previous studies of the effect of aerosol particles on cirrus clouds because it includes an explicit representation of the relevant physics (Penner et al., 2009; Penner et al., 2018) and Penner et al. (2018) added the capability to represent evaporation of water in downdrafts. However, in the KL parameterization, aerosol particles in different size bins will freeze chronologically from the largest size bin until the rate at which RHi decreases by water vapor deposition equals the rate at which RHi increases as a result of temperature decreases. Under this assumption,

competition among different aerosol size bins for water deposition is not allowed. As a result, the homogeneous freezing of some particles in small size bins is underestimated in KL parametrization (Liu and Shi, 2018). The KL parametrization results in a smaller sensitivity to increases in sulfate aerosol number than the LP and BN parametrizations except at very low sulfate number concentrations, while the three parameterizations have similar sensitivity to the number concentration of INPs (Shi and Liu, 2018).

Global numerical simulation experiments of aerosol effects on cirrus cloud formation have been carried out in a limited number of studies with different ice nucleation parameterizations and updraft treatments. Penner et al. (2009) used the KL and LP parameterizations to estimate the radiative forcing of aerosols on cirrus clouds using an off-line ice nucleation and radiative transfer model. They found a negligible forcing from sulfate but a significant cooling (ranging from -0.38 to -0.56 W m^{-2}) from surface-based and aircraft emissions of soot with the assumption that 100% of soot particles are efficient INPs (Penner et al., 2009). As a result, the radiative forcing of all anthropogenic aerosols was estimated to be -0.53 to -0.67 W m^{-2} using the LP and KL parameterizations. However, observations later indicated that only 0.01 to 0.1% of the less-hygroscopic soot from fossil fuels and biomass fires act as good INPs at supersaturations near 140% RHi and low temperatures (Koehler et al., 2009; Pratt et al., 2011; Prenni et al., 2012). Gettelman et al. (2012) used the LP and BN parameterizations and calculated that the radiative forcing associated with aerosol effects on cirrus clouds is 0.27±0.10 W m^{-2} (the uncertainty is the standard deviation of the interannual variations hereafter) as a consequence of increasing anthropogenic sulfur emissions (with no effect from soot) (Gettelman et al., 2012).

In addition to assumptions of the extent to which soot might act as an INP, a second source of uncertainty in the calculation of aerosol forcing in cirrus clouds is the treatment of the sub-grid scale updraft velocity used in the nucleation scheme (Zhou et al., 2016). Penner et al. (2009) used a normal probability distribution with a standard deviation of 0.33 m s^{-1} (Penner et al., 2009) while Wang and Penner (2010) used a single updraft velocity based on the standard deviation of mesoscale temperature fluctuations associated with gravity waves (Wang and Penner, 2010). Other models chose a sub-grid scale updraft velocity associated with the predicted turbulent kinetic energy (Liu et al., 2012; Kärcher and Lohmann, 2002; Lohmann, 2002; Lohmann et al., 1999). Kuebbeler et al. (2014) added the effect of the contribution of orographic waves to the vertical velocity. Penner et al. (2018) first used a wave spectrum (instead of a constant updraft velocity) together with the KL parameterization to treat the formation of ice crystals. They used the equatorial spectrum of observed gravity waves presented by Podglajen et al. (2016) together with the seasonal and latitudinal variations determined by Gary (2006) and Gary (2008). They also varied the standard deviation from Podglajen et al. (2016) based on the vertical stratification of atmospheric stability, the atmospheric density and topography. However, the radiative forcing of sulfate as well as all anthropogenic aerosols were not explored due to the deficiencies in the KL parameterization (Liu and Shi, 2018).

Secondary organic aerosols (SOA) have been shown to have a highly viscous semisolid or even glassy state at low temperatures and low RHi in many experiments (Koop et al., 2011; Pajunoja et al., 2014; Renbaum-Wolff et al., 2013; Saukko et al., 2012). Observations also found SOA acting as IN and in the ice crystal residues of cirrus clouds (Ignatius et al., 2016; Wagner et al., 2017; DeMott et al., 2003; Cziczo et al., 2013; Wilson et al., 2012). A peak in the number concentration of ultrafine

particles were observed near 12km in the Amazon and identified as primarily organic. Furthermore, a marker molecule indicated that a substantial fraction of the organics in aerosol-rich layers in the upper troposphere were associated with the oxidation of isoprene (Andreae et al., 2018). A modelling study that included the nucleation of new particles through organic nucleation predicted that there are a large number of accumulation mode SOA particles existing in the upper tropical troposphere which may be important for the ice nucleation (Zhu and Penner, 2019). SOA particles have a strong potential to act as INPs to form ice particles via heterogeneous freezing under the conditions conducive to ice formation in the upper troposphere (Knopf et al., 2018). However, the influence of SOA on cirrus clouds is not yet fully studied (but see Penner et al., 2018).

In this study, we combined the best features of the LP and KL parameterizations to develop a hybrid ice nucleation scheme that accounts for the changes in ice number concentrations in both the updrafts and downdrafts associated with a spectrum of gravity waves. Using a global climate model coupled with the new ice nucleation scheme, the radiative forcing of aircraft soot and sulfate were examined. Furthermore, the radiative forcing of anthropogenic aerosols on cirrus clouds since the PI time period was estimated both including and excluding the effect of changes in SOA. A global average negative anthropogenic forcing of -0.20±0.05 W m^{-2} without SOA as a result of aerosol effects in cirrus clouds is suggested. The forcing is reduced to -0.04±0.08 W m^{-2} when SOA is included.

2. Methodology

2.1 Model

We used the Community Earth System model (CESM) version 1.2.2 (refer to http://www.cesm.ucar.edu/models/cesm1.2/ for details) coupled to the University of Michigan IMPACT aerosol model (Liu et al., 2005 with updates as described herein) with a resolution of 1.9° (longitude)×2.5° (latitude) and 30 vertical layers to simulate aerosols and their effects on cirrus clouds. This version of the IMPACT model simulates the number and mass of pure sulfate in three modes (i.e. nucleation (<5 nm), Aitken (5-50 nm) and accumulation (>50 nm)) and their interaction with the following fourteen other aerosol species/types. Sulfate is the only aerosol participating in homogeneous ice nucleation in the model. Soot from fossil fuel and biofuel burning (fSoot) is simulated in three modes with different hygroscopicity according to the number of monolayers sulfate on its surface (Yun et al., 2013) while soot from biomass burning (bSoot) is simulated in one mode. 0.05% of fSoot with <1 monolayers of sulfate and 0.1% of fSoot coated with 1-3 monolayers of sulfate as well as 0.1% of bSoot are assumed to be effective INPs. The hygroscopicity of fSoot and bSoot is determined by volume averaging the hygroscopicity of the underlying particles and the number of sulfate monolayers on the particles. Aircraft soot is simulated in two modes. The first mode has acted as an ice nuclei within contrails that subsequently evaporated (cSoot). The 2nd mode which has not been an ice nuclei within contrails is not considered to act as an INP in the model. We assume the soot that has already been included in contrail ice is pre-activated and coated with less than 3 monolayers of sulfate, is assumed to be an INP similar to the treatment in Zhou and Penner (2014) (see also Mahrt et al., 2019). Dust and sea salt are each carried in four separate bins with varying radii. Dust with fewer than 3 monolayers of sulfate coating is used to form heterogeneous INP in the model. This

treatment is consistent with the results of field studies by DeMott et al. (2003), Cziczo et al. (2004) and Richardson et al. (2007). The assumptions for aerosols to be effective INPs in the model are summarized in Table 1. The aerosols simulated by the IMPACT model are only able to nucleate the initial ice crystal number concentration in cirrus clouds in the CESM model. Thereafter, the growth and sedimentation as well as evaporation of ice crystals follow the treatment in the CESM. In addition, the changes to cirrus clouds have feedbacks as a result of changes to the radiation budget, temperature, and the formation of warm clouds, as simulated in the CESM model.

2.2 Ice nucleation parameterization

The LP parameterization is only able to calculate the ice nucleation in a rising parcel, but is not able to predict the changes in the supersaturation or simulate the evaporation of ice in downdrafts. As a result, the scheme used by Penner et al. (2018) to treat gravity waves cannot be used with the LP parameterization as it was originally formulated. The KL scheme calculates the changes in the sub-grid scale variation of RHi in a cloud parcel as a result of updrafts or downdrafts and the growth or decay of ice particles. Unlike some schemes (e.g. Shi et al., 2015) which consider that the initial nucleation in an updraft takes place in the presence of ice from the previous time step, we assume the first parcel updraft within a GCM time step does not carry any preexisting ice, but thereafter if ice forms it may either grow and decrease the supersaturation or evaporate adding water vapor to the parcel. However, aerosols freeze in the order of size bins and this neglects the competition among different aerosol size bins, which results in an underestimation of the ice formed from aerosols in small size bins and a low sensitivity to the change of aerosol number

(Liu and Shi, 2018). In this study, we combined the LP and KL parameterizations to develop a new ice nucleation scheme (hereafter HYBRID) to make use of their strengths and avoid their defects.

In the HYBRID scheme, the supersaturation (S_i) in the cloud parcel is calculated explicitly using the KL scheme so that ice particles are able to grow or decay throughout the time variations in the updrafts and downdrafts associated with gravity waves. S_i is calculated as a function of the updraft and aerosol concentrations at each grid. S_i is updated every second using

$$\frac{dS_i}{dt} = a_1 S_i w - (a_2 + a_3 S_i) \int_0^\infty dr_0 \frac{dn}{dr_0} R_{im}(r_0)$$

where the parameter a_1 is given by $a_1 = (L_s M_w g)/(c_p R T^2) - Mg/(RT)$, with the molar mass of air M and water M_w, latent heat of sublimation L_s, constant of gravity g, heat capacity at constant pressure c_p, the universal gas constant R, and air temperature T. w is the vertical velocity. a_2=1/n_{sat} with the water vapor number density at ice saturation n_{sat}. $a_3 = L_s^2 M_w m_w/(c_p p T M)$, with the mass of a water molecule m_w and the air pressure p. R_{im} is the monodisperse freezing/growth integral,

$$R_{im} = \frac{4\pi}{v} \int_{-\infty}^{t} dt_0 \dot{n}_i(t_0) r_i^2(t_0, t) \frac{dr_i}{dt}(t_0, t),$$

where v is the specific volume of a water molecule. $dt_0 \dot{n}_i(t_0)$ is the number density of aerosol particles that nucleate ice and freeze within the time interval between t_0 and $t_0 + dt_0$, $r_i(t_0, t)$ is the radius of the spherical ice particle at time t that froze and commenced to grow at time $t < t_0$, and dr_i/dt is the radial growth rate of that ice particle. In the HYBRID scheme, $\dot{n}_i(t_0)$ is determined using the LP parameterization.

A series of updraft velocities at each grid point was generated based on a fitted wave spectrum to the observed equatorial gravity waves from Podglajen et al. (2016). The standard deviation of this wave spectrum was extended to other latitudes and

seasons by using the parameterization proposed by Gary (2006, 2008). It was extended vertically based on the static stability, atmospheric density and topography. This parameterization of the wave spectrum associated with gravity waves is described in Penner et al. (2018).

When the updraft velocity is positive, the LP parameterization is used to calculate the increase in the ice number from homogeneous and/or heterogeneous freezing, so that the HYBRID scheme avoids the lack of sensitivity to changes in aerosol number in the KL parameterization when calculating the number of new ice particles. The LP parameterization is derived by fitting the results of a large set of parcel model simulations covering different conditions in the upper troposphere (Liu and Penner, 2005). Two separate regimes are identified by the sign of $T - 6.07 \ln w + 55.0$ (where T is the temperature and w is the updraft velocity) to calculate the change of *Ni* due to homogeneous nucleation. When the sign is positive, the solution is in fast-growth regime which is associated with higher T and lower w. The number concentration of new ice crystals (N_i or $\dot{n}_i(t_0)$ as in the above) is then calculated with the following equation

$$N_i = min\{exp(a_2) N_a^{a_1} exp(bT) w^c, N_a\}$$

where $b = b_1 lnN_a + b_2$, and $c = c_1 lnN_a + c_2$. N_a is the number concentration of sulfate in the Aiken and accumulation modes. The coefficients a_1, a_2, b_1, b_2, b_3, c_1, c_2 are constant, and can be found in Table 1 of Liu and Penner (2005). For lower T and higher w (the slow-growth regime), the following equation is applied to calculate N_i:

$$N_i = min\{exp[a_2 + (b_2 + b_3 lnw)T + c_2 lnw] N_a^{a_1 + b_1 T + c_1 lnw}, N_a\}$$

where the coefficients a_1, a_2, a_3, b_1, b_2, b_3, c_1, c_2 are again listed in Table 1 of Liu and Penner (2005) and are different from those in the fast-growth regime. The

number concentration of N_i from INPs in the heterogeneous nucleation regime is given as

$$N_i = min\{exp(a_{22})N_{INP}^{b_{22}} exp(bT)w^c, N_{INP}\}$$

where $b = (a_{11} + b_{11} lnN_{INP})lnw + (a_{12} + b_{12} lnN_{INP})$ and $c = a_{21} + b_{21} lnN_{INP}$. N_{INP} is the number concentration of total INPs. The coefficients a_{11}, a_{12}, a_{21}, a_{22}, b_{11}, b_{12}, b_{21}, b_{22} can be found in the Section 4.2 of Liu and Penner (2005). When the updraft velocity is low and temperature is high, heterogeneous ice nucleation takes place initially and depletes the water vapor in the parcel so that homogeneous ice freezing never occurs. The threshold temperature T_c for heterogeneous nucleation-only is given by

$$T_c > aln(w) + b$$

where $a = -1.4938ln(N_{INP}) + 12.884; b = -10.41ln(N_{INP}) - 67.69$. When the regime is in a transition from heterogeneous-dominated to the homogeneous-dominated regimes, the total ice number concentration from nucleation can be higher than the ice concentration from only heterogeneous nucleation, but lower than that from the pure homogeneous nucleation case. Then, N_i is interpolated from

$$N_i = N_{Het}\left(\frac{N_{Het}}{N_{Hom}}\right)^{\frac{N_{INP}-N_c}{0.9N_c}}$$

where N_{Het} is the ice number from pure heterogeneous nucleation, N_{Hom} is the ice number from pure homogeneous nucleation, N_{INP} is the number concentration of INPs and N_c is the critical number concentration of INPs for the heterogeneous nucleation-only regime.

Based on the method outlined above, HYBRID scheme calculates the increase in *Ni* using LP parameterization. The new ice crystals from nucleation either grow or decay with consumption/evaporation of water vapor and therefore change *Si*,

which is determined using KL parameterization. The changes in *Si* then influence which particles are able to nucleate forming ice crystals.

We define cirrus clouds for which the effects of aerosols are defined/calculated as all large-scale clouds formed at temperatures < -35°C. Cirrus clouds at these temperatures include anvil cirrus that are formed by the outflow from deep convection as well as large-scale cirrus formed by in-situ gravity waves. The detrained ice crystal number concentration in anvils is calculated from the detrained ice mass by assuming a spherical particle with a constant volume-mean radius, which is approximated as $3\rho_0 Q/(4\pi\rho_i r_{iv}^3)$ following Lohmann (2002). ρ_i is the ice crystal density, ρ_0 is the air density, r_{iv} is the volume mean radius determined from a temperature-dependent lookup table (Kristjánsson et al. 2000; Boville et al. 2006), Q is the detrainment rate of cloud water mass diagnosed from the convection parameterization. The new clouds generated by convective detrainment are assumed to be at saturation with respect to ice. In doing this, anvil clouds and in situ cirrus compete for the available water vapor within a grid box. When anvil clouds are formed due to convective detrainment, it reduces the saturation ratio in the clear-sky portion of a grid, and can potentially reduce the frequency of in situ large-scale cirrus formation (Wang and Penner 2010; Wang et al. 2014). We only calculate *Ni* as a result of the nucleation of aerosol in large-scale cirrus, so that when anvils occur in a grid box, we average the concentrations to determine the total ice number concentration in cirrus clouds. Anthropogenic emissions contribute to the change in the number concentration of ice crystals in large-scale cirrus cloud, but these are then averaged with the crystals in anvils.

2.2.1 Evaluation of the HYBRID scheme

In order to examine the ability of the HYBRID ice nucleation scheme to simulate ice number concentration, the results from a box model using the HYBRID

scheme are compared with those from an adiabatic parcel model under the same simulation conditions. The adiabatic parcel model was that used to generate the LP parameterization and was introduced in Liu and Penner (2005). The two models are run for 30 min for each simulation, which is the time step used in the CESM. During the 30 min, the updraft velocity is updated every 2.2 min as recommended by Podglajen et al. (2016). The ice number concentrations after the 30 min simulation from the two models are compared. We ran both the adiabatic parcel model and the HYBRID box model using a constant updraft velocity for each 2.2-min interval. When the velocity is positive ice crystals form and grow in the HYBRID box model as described above. For downdrafts, if the supersaturation is below 100%, the two models use the same method to simulate the evaporation of any existing ice particles, which is also the same method used in the global model as suggested in Kärcher et al. (2006). The scheme used here for the HYBRID box model is the same as the HYBRID scheme used in the global model. Note that the final interval within each 30 minute simulation is shortened in order to match the treatment used in the CESM/IMPACT model which uses a 30 minute time step. When run within the CESM model, this final ice number concentration is then passed back to the CESM model after this 30 minute interval.

The updrafts and downdrafts associated gravity waves are determined from a Laplace distribution as suggested by the fit to the observed gravity waves by Podglajen et al. (2016). We conducted 10,000 simulations using a random selection of the updrafts and downdrafts for each model. Both models use the same selection of updrafts and downdrafts in each simulation. We set up an initial condition with a temperature of 230K, the standard deviation for the updraft velocities was 0.5 m s^{-1} and the initial RHi was 130%. The sulfate number concentration was set to 0.2 L^{-1}

while the dust concentration was 10 L^{-1}. These particles then participate in either homogeneous nucleation or heterogeneous immersion nucleation.

Figure 1 shows a histogram of the predicted ice number concentration (*Ni*) for 10,000 simulations of the adiabatic parcel model and the box model using the HYBRID scheme. Two populations of *Ni* are shown in Figure 1. The lower population (with concentrations of the order of 10 L^{-1} or less) represents primarily heterogeneous nucleation on dust particles, while the higher population (with concentrations of the order of 10^2 L^{-1} or more) represents primarily homogeneous nucleation on sulfate aerosols. The results in the simulations dominated by heterogeneous nucleation are mostly similar for the two models, although the HYBRID scheme overestimates the Ni between 1~10 L^{-1} when the results from the adiabatic parcel model are less than 10^{-1} L^{-1} for some of these same simulations. The average *Ni* from heterogeneous nucleation over 10,000 simulations from the adiabatic parcel model is 9.40±2.31 L^{-1}, while that from the HYBRID scheme is 9.52±2.08 L^{-1}.

The box model using the HYBRID scheme predicts larger Ni from homogeneous nucleation than the parcel model in the 88% of simulations where homogeneous nucleation occurs. There are more simulations using the HYBRID scheme that predict larger Ni from homogeneous nucleation than the parcel model as indicated by larger number of counts of large *Ni* (10^4 L^{-1} or more) in Figure 1. The HYBRID scheme uses the LP parameterization for every small time step of 2.2 min. Since the LP parameterization was built using the largest Ni in an ascending parcel after 30 min, there is a tendency for the HYBRID scheme to overpredict *Ni*. The average *Ni* from homogeneous nucleation over the 10,000 simulations in the two models is 1.41±4.23 L^{-1} from the parcel model, while it is 1.52±4.83 L^{-1} from the HYBRID model. The HYBRID scheme overestimates the Ni from homogeneous

nucleation by 7.4%, which dominates the difference in total Ni between two models. Overall, the average total Ni over the 10,000 simulations is 1.53±4.83 L^{-1} using the HYBRID scheme, which is 7.3% larger than the result from the parcel model (1.42±4.23 L^{-1}). We also examined the difference between the above case when sulfate was 200 cm^{-3} compared to when sulfate was 20 cm^{-3}, and the difference was within 7.2% of that using the full parcel model. Although the HYBRID scheme predicts a somewhat larger number of nucleated ice particles, on average, the results are reasonable compared to the results from the parcel model.

2.3 Experiments with the global model

We performed a series of model experiments in which different emissions of aerosols and aerosol precursors are used. Table 2 provides a summary of these experiments. The base case (PD_Base) uses emissions for the present day (PD, for the year 2000) for anthropogenic sulfur and soot from fossil fuel adopted from Community Emission Data System (CEDS) (Hoesly et al., 2018). Emissions from van Marle et al. (2017) are adopted for biomass burning emissions. These emissions are the same as the emissions datasets used for the CMIP6 simulations. The year 2000 emissions are used for all years of our simulation. We included soot from aircraft for 2006 based on the Aviation Environment Design Tool (AEDT) data set (Barrett et al., 2010). The AEDT data are presumed to be more accurate than the CMIP6 aircraft emissions since they were developed based on the original flight tracks of each of 31 million commercial flights worldwide (Wilkerson et al., 2010). The dimethylsulfide (DMS) emissions from the ocean are assumed constant in the PD and PI periods (Tilmes et al., 2016). The emission of dust uses the scheme from Zender et al. (2003). In a sensitivity experiment (PI_cSoot), the emission of cSoot is

removed from PD_Base to examine its impact on ice number concentration and radiative forcing. We also set a case (PI_SO4) with the emission of anthropogenic sulfur changed to PI (≈1750) to calculate the radiative forcing of sulfur. The case PI_ALL set all emissions to those of the PI period (≈1750) to examine the radiative forcing of all anthropogenic aerosols on cirrus cloud. Additionally, we set up two experiments to examine the effect of SOA as an INP on anthropogenic forcing in cirrus clouds. The case PD_SOA and PI_SOA adds newly nucleated SOA particles that have grown to the accumulation mode as additional INPs to the cases of PD_Base and PI_ALL. The cases including SOA in the PD and PI read in the explicit number concentration of newly formed SOA in the accumulation mode nucleated from highly oxygenated organic molecules (HOMs) that form from the oxidation of α-pinene. The nucleated SOA particles grow by deposition and coagulation of sulfuric acid as well as the oxidation products of isoprene, α-pinene, limonene and aromatics, that are in the aerosol phase. This SOA was simulated using the version of the CESM/IMPACT model outlined in Zhu et al. (2017, 2019) and Zhu and Penner (2019, 2020). The SOA that meets the requirements of the glass transition temperature and RHi calculated using the equations in Wang et al. (2012) acts as an effective heterogeneous INP.

The changes in aerosol emissions only influence the number concentration of ice nuclei in the CESM, and thereby give the indirect radiative effect in cirrus clouds. The direct radiative effect caused by the change of aerosols is not included. Clear sky radiative forcing in this study is not associated with direct aerosol radiative forcing, but is rather mainly due to changes in water vapor which leads to changes in the clear sky longwave radiation (Wang and Penner, 2010). All cases were run with prescribed sea surface temperatures for the present day and winds were nudged towards ECMWF reanalysis data for the years 2005-2011 using a nudging time of 6

hours (Zhang et al., 2014). The data for the last six years were used for analysis in this study.

3. Results from the global model

3.1 Ice number concentrations

The predicted Ni in PD_Base case is compared with the observed Ni reported by Krämer et al. (2009) and Krämer et al. (2020) in Figure S1. Data from the model have been selected to have ice water mixing ratios > 10^{-8} kg kg^{-1} to match values seen in the in-situ observations (Krämer et al., 2016). The global model using the HYBRID scheme is able to do a reasonable job in predicting Ni with the difference in the median value between the simulation and observation less than 50% for all temperatures except for the high concentrations seen between 197K and 213K. The model predicts ~3 times higher *Ni* on average compared to the observations between 197K and 213K. Although the comparison of ice number concentration between our model and observation has not improved significantly compared to that shown by Penner et al. (2018), the new nucleation scheme improves the ability of nucleation to occur on small sized particles, since it avoids the calculation of ice nucleation chronologically from large sizes to small size used in the KL scheme, which results in an underestimation of ice crystals formed from small size particles.

The global average *Ni* in the PD_Base is 0.15×10^{10} m^{-2} with the largest *Ni* in the tropics of Eastern Hemisphere (Figure 2a). Most ice particles nucleate in the upper troposphere (150~200 hPa) in the tropics, while some ice nucleation occurs in the lower troposphere (around 300 hPa) in the polar regions (Figure 2b). The ice particles formed from homogeneous nucleation dominate the total *Ni* in most regions over the world (Figure S2a) and are responsible for ~95% of global average

Ni (Figure 2c). The large number concentration of sulfate in the Aitken and accumulation modes in the upper troposphere over the west Pacific Ocean and north Indian Ocean contributes to the remarkably large *Ni* in the tropical Eastern Hemisphere. Heterogeneous nucleation dominates the *Ni* in the northern middle-high latitudes where anthropogenic soot emission is high (Figure S2a), although the *Ni* from heterogeneous nucleation is high in the tropics (Figure 2e). Homogeneous nucleation mostly occurs in the upper troposphere (around 200hPa in the tropics and around 300hPa in the extratropical regions), while heterogeneous nucleation is an important contributor to *Ni* in the middle and lower troposphere (Figure S2b). Although the Ni from homogeneous nucleation is high, the occurrence frequency of homogeneous nucleation (calculated as the ratio of the time steps when homogeneous nucleation occurs to all time steps with nucleation occurring) is up to ~20% in the tropics and < 5% in most other regions (Figure S2c).

The competition between the heterogeneous INPs and homogeneous haze particles determines the change in *Ni* between the PD and PI periods. We set up three sensitivity cases to separately examine the effects of the emission of cSoot for aircraft, anthropogenic sulfur and all anthropogenic emissions on *Ni*. INPs always nucleate prior to homogeneous nucleation in a rising air parcel, so they consume the available water vapor and inhibit homogeneous freezing when added to regions dominated by homogeneous nucleation. The *Ni* formed from heterogeneous nucleation increases significantly around 200hPa over the world due to the inclusion of INPs from cSoot, especially near Southeast Asia (Figure 3e, 3f). Simultaneously, homogeneous nucleation is inhibited significantly around 200hPa in Southeast Asia and other tropical regions (Figure 3c, 3d). The emissions of aircraft soot that form contrails peak near 200hPa with the spatial distribution shown in Figure 1a in the Zhou and Penner (2014). Due to the much larger decrease in *Ni* from homogeneous nucleation than the increase in *Ni* from heterogeneous nucleation, the global average

482 *Ni* is decreased by 0.1×10^8 m^{-2} (1%) when including the emission of aircraft soot
483 (Figure 3a). The change in *Ni* due to cSoot is small with a significant change only
484 over the North Atlantic Ocean and east coastal regions in North America (Figure 3a).

485 In contrast to the case of aircraft soot, the increase in the sulfur emissions from
486 PI to PD leads to a large increase in *Ni* from homogeneous nucleation in most regions,
487 which causes an increase of 1.01×10^8 m^{-2} in the global average *Ni* (Figure 4c). The
488 increase in *Ni* from homogeneous nucleation contributes to the significant increase
489 in *Ni* near 150hPa over South Asia, Africa and the North Indian Ocean (Figure 4a).
490 The decrease in *Ni* from heterogeneous nucleation offsets some of the increase in *Ni*
491 from homogeneous nucleation and leads to a significant decrease in *Ni* near 300hPa
492 over the North Pacific Ocean (Figure 4a). In total, the global average *Ni* is increased
493 by 0.73×10^8 m^{-2} (5%) due to the increase in sulfur emissions.

494 The change in *Ni* from PI to PD due to all anthropogenic emissions is a balance
495 among the effects of increasing INPs from surface emissions and aircraft soot as
496 well as the increase in haze particles. The effect of all anthropogenic emissions on
497 *Ni* is mostly dominated by the increase in *Ni* from homogeneous nucleation caused
498 by the increase in sulfur emissions, but homogeneous nucleation is inhibited
499 somewhat by increased INPs from soot (compare Figure 5c and 4c). As a result, the
500 global average increase in *Ni* from homogeneous nucleation between PD_Base and
501 PI_ALL is only 58% of that between PD_Base and PI_SO4. The change in *Ni* from
502 heterogeneous nucleation is decreased in the mid-high latitudes of the Northern
503 Hemisphere (NH) from PD_Base to PI_ALL similar to the decrease from PD_Base
504 to PI_SO4 (Figure 5e, 5f). However, the increase in INPs from soot near Southeast
505 Asia leads to a small increase in *Ni* from heterogeneous nucleation there (Figure 5e).
506 In total, the increase in all anthropogenic emissions causes a significant increase of
507 *Ni* in South Asia and the North Indian Ocean while a significant decrease of *Ni* is

found in mid-latitude regions and some Arctic regions, resulting in 0.49×10^{8} m^{-2} (3%) more *Ni* from PI to PD for the global average.

It is conspicuous that sulfur and aircraft soot emissions have effects with different signs for the change in *Ni* (Figure 3a, 4a). Generally, INPs from aircraft soot decrease *Ni* due to the suppression of homogeneous nucleation in the regions dominated by homogeneous nucleation, while the increase in sulfur emissions increases *Ni* in these same regions due to the enhancement of homogeneous nucleation. However, the changes to *Ni* have opposite signs in the west Pacific Ocean off the coast of Southeast Asia, where the homogeneous nucleation is most active (Figure 2c). We attribute this to the possible effect of aerosol and cloud feedbacks to the meteorological state. When including aircraft soot, the temperature is decreased (Figure S3b) and the RHi is increased (Figure S3a) around 150hPa over the west Pacific Ocean, where *Ni* from homogeneous nucleation increases a lot (Figure 3c). The decrease in temperature is beneficial to homogeneous nucleation. Meanwhile, the emission of aircraft soot is very low in the west Pacific Ocean due to the lack of flight routes there (refer to Figure 1a in Zhou and Penner (2014)), so that the effect of aircraft soot on the suppression of homogeneous nucleation is weak in that region (Figure 3e). As a result, the *Ni* from homogeneous nucleation is increased, which determines the increase in the *Ni* near 150 hPa over the west Pacific Ocean due to the emission of aircraft soot (Figure 3a). Similarly, when the sulfur emissions are increased from PI to PD, the change in cirrus clouds influences the meteorological state. A large decrease in RHi at 150hPa is found in the west Pacific Ocean (Figure S4a), so that the occurrence frequency of homogeneous nucleation decreases when sulfur emissions increase (Figure S4d). Additionally, the temperature at 150hPa increases over the world (Figure S4b), which also contributes partly to the decrease in the occurrence frequency of homogeneous nucleation.

Although global sulfur emissions increase sharply from PI (2.2 Tg S $year^{-1}$) to PD (55 Tg S $year^{-1}$), the anthropogenic emissions mainly occur on the mainland with much smaller emissions over the ocean even though the sulfur emissions from shipping increase by 6.4 Tg S $year^{-1}$. The column number concentration of sulfate having the potential to freeze homogeneously do not increase significantly over most ocean regions (Figure S4c), so that the decrease in the occurrence frequency of homogeneous nucleation leads to a decrease in *Ni* from homogeneous nucleation over the west Pacific Ocean (Figure 4c). The increase in the temperature in the upper troposphere over the world (Figure S4b) also partly explains the decrease in *Ni* from heterogeneous nucleation when only sulfur emissions increase (Figure 4e). The feedbacks to the meteorological state in remote regions always have an opposite effect on the changes in *Ni* compared to the effect in regions with large anthropogenic emissions. These meteorological feedbacks partly reduce the changes in global average *Ni* due to anthropogenic emissions. Although these opposite changes in *Ni* due to meteorological feedbacks are not statistically significant (Figure 3a, 4a, 5a), our conjecture based on the model results indicates that the meteorological feedbacks caused by the radiative effects of aerosols might contribute to the change in *Ni* in remote regions. These important feedback processes need to be investigated further.

3.2 Radiative forcing

The decrease in *Ni* in the upper troposphere usually leads to an increase in the size of ice particles, which promotes the gravitational removal and formation of snow, causing a decrease in the ice water path (IWP) and vice versa. As a result, the change in IWP is mainly determined by the change in *Ni* and have a similar

559 geographic pattern. The global average IWP in the model is 14.6 g m^{-2} for the
560 PD_Base case, which is lower than that observed in different CloudSat/CALIPSO
561 analyses (21~28 g m^{-2}) (*Li et al.*, 2012). We used a cut off diameter of 250 μm to
562 move cloud ice to snow. A cutoff diameter of 400 μm in the model almost doubles
563 the IWP in our model (compare IWP of dbfc_mg10 and dbfc in Table 3 in Penner et
564 al., 2018). The emission of aircraft soot leads to a significant decrease in IWP in
565 Southeast Asia and the East coast of North America, caused by the inhibition of
566 homogeneous nucleation (Figure 6a). As shown in Figure 6c, the increase in the
567 sulfur emissions leads to a significant increase in IWP in the north Indian Ocean due
568 to the changes in *Ni* from homogeneous nucleation. The decrease in IWP in East
569 Asia and the Arctic is attributed to the decrease in *Ni* from heterogeneous nucleation
570 (Figure 6c). The geographic pattern of changes in IWP due to the change in all
571 anthropogenic emissions from PI to PD is dominated by the changes in IWP caused
572 by the changes in sulfur emissions (compare Figure 6c and 6e). However, the
573 increase in IWP in tropical regions is smaller and the decrease in IWP in the middle
574 and high latitudes of the NH is more negative in the PD_Base-PI_ALL case
575 compared to the PD_Base-PI_SO4 case because of the inhibition of homogeneous
576 nucleation caused by the increase in the emission of surface and aircraft soot. As a
577 result, although the geographical pattern of the changes in IWP is similar for the
578 PD_Base-PI_ALL and PD_Base-PI_SO4 cases, the magnitude of changes in the
579 global average IWP switches from positive (0.07 g m^{-2} for PD_Base-PI_SO4, Figure
580 6c) to negative (-0.13 g m^{-2} for PD_Base-PI_ALL, Figure 6e).

581 The changes in *Ni* and IWP lead to a change in the cirrus cloud fraction and also
582 feedback to produce a change in the lapse rate of temperature, which has an effect
583 on the delivery of water vapor and the strength of convection and these changes
584 influence the formation and lifetime of liquid water clouds. The liquid water path

585 (LWP) changes due to these complex dynamical feedbacks are shown in Figure 6b,
586 6d and 6f. The changes in LWP are all less than 0.5% with only a small number of
587 grids with a significant change. The changes in the shortwave and longwave
588 radiative fluxes are determined by the changes in LWP and IWP (as well as the
589 change in *Ni*), although they are dominated by the change in IWP. The changes in
590 aerosol only have a direct effect on the cirrus clouds in our model, while the changes
591 in warm clouds are caused by feedbacks due to the change in cirrus clouds. The
592 changes in the all-sky shortwave radiative forcing (SRF) and longwave radiative
593 forcing (LRF) at the top of the atmosphere (TOA) generally follow the changes in
594 IWP but have the opposite sign (Figure 7, Figure 8 and Figure 9). The changes in
595 LWP could either enhance or offset the effect of changes in IWP on the radiative
596 fluxes depending on whether the sign of the changes in IWP and LWP are
597 reinforcing or not. The emission of cSoot leads to a positive global average SRF due
598 to the significant increase in shortwave radiative fluxes off the coast of East Asia
599 and over the North Indian Ocean, while and the significant decrease in the longwave
600 radiative fluxes over East Asia, the North Indian Ocean and North Atlantic Ocean
601 contribute to a negative global average LRF mostly due to the decrease in the global
602 average IWP (Figure 7). On the other hand, the increase in sulfur emissions causes
603 a negative global average SRF largely due to the significant decrease over South
604 Asia, North Africa and the North Indian Ocean (Figure 8a). Simultaneously, the
605 increase in the IWP in these regions leads to a significant increase in longwave
606 radiative fluxes resulting in a positive global average LRF, although the LRF is
607 significantly negative in the middle to high latitude over the east coast of Asia.
608 (Figure 8b). The changes in the SRF and LRF due to the increase in all anthropogenic
609 emissions have a similar geographic pattern to those caused by the increase in sulfur
610 emissions but the global average forcings have opposite signs (compare Figure 8c,
611 8d and Figure 9c, 9d). This is due to the decrease in the global average IWP caused

612 by the inhibition of homogeneous nucleation as a result of the increased emissions
613 of soot.

614 The total all-sky net forcing (NRF) is determined by the balance between SRF
615 and LRF. The radiative effects in cirrus clouds are dominated by longwave radiative
616 effects. However, it is still possible that the radiative forcing due to changes in *Ni* in
617 cirrus clouds in some regions is dominated by SRF due to the combined effects on
618 shortwave forcing from the changes in cirrus clouds together with changes to warm
619 clouds caused by feedbacks. The emission of cSoot has a negative global average
620 NRF of -0.14±0.07 W m^{-2} in cirrus clouds with only a few significant grids, although
621 the SRF and LRF due to cSoot are significant in some coastal regions off of East and
622 South Asia (Figure 7). The NRF due to cSoot is most negative around the 30°N
623 where the emission of aircraft soot is high, while there is a small positive forcing
624 around 10°N dominated by SRF (Figure 7f). The NRF is the sum of the clear sky net
625 radiative forcing (NRFC) and the cloud radiative forcing (CRF) caused by changes
626 in cSoot. The global average CRF is -0.10±0.07 W m^{-2}, which dominates over the
627 NRFC and explains 72% of the NRF of cSoot (Figure 7c, 7d).

628 Although the increase in sulfur emissions from PI to PD leads to an increase in
629 the global average *Ni* and IWP, the global average NRF due to sulfur emissions is
630 near zero, -0.02±0.06 W m^{-2}. The NRF due to sulfur emissions is significant and
631 positive (up to 7.1 W m^{-2}) around the 30°N in South Asia and North Africa (Figure
632 8e). The NRF is negative over most mid to high latitudes of the NH, which is
633 attributed to the decrease in LRF associated with the feedback to the decrease in *Ni*
634 from heterogeneous nucleation there. However, the significant negative NRF in the
635 north Indian Ocean and positive NRF in the west Pacific Ocean are dominated by
636 the change in SRF (Figure 8a, 8e). The LWP increases in the north Indian Ocean as
637 a result of dynamic feedbacks from the changes in the cirrus clouds, leads to the

significant SRF together with the changes in IWP and cirrus clouds. The negative NRF in the north Indian Ocean and mid to high latitudes of the NH offset the positive NRF around the 30°N (Figure 8e). The significant negative NRF over the North Indian Ocean is dominated by the CRF, while the significant positive NRF over South Asia and North Africa is the combined effect of CRF and NRFC. The global average CRF is -0.17±0.06 W m^{-2} and determines the sign of the global average NRF. However, the global average NRFC is 0.14±0.02 W m^{-2} with a wide area of positive values over the NH, which offsets most of CRF.

Compared to the NRF due to the increased sulfur emissions, the NRF is less positive in South Asia and more negative over the mid to high latitudes of the NH and the north Indian Ocean when including the increased emissions of surface and aircraft soot as well as sulfur together (Figure 9e). In the mid to high latitudes of the Southern Hemisphere (SH), SRF and LRF always cancel each other so that NRF is negligible. As a result, the global average NRF due to the all increased anthropogenic emissions from PI to PD is -0.20±0.05 W m^{-2}, which is mainly dominated by the changes in LRF (Figure 9e, 9f). Both the CRF and NRFC due to all anthropogenic emissions are largely explained by the CRF and NRFC caused by change in emission of sulfur (compare Figure 9c, 9d and Figure 8c, 8d). The global average CRF is -0.28±0.04 W m^{-2} due to the changes in all anthropogenic emissions, while the NRFC is slightly positive (0.08±0.02 W m^{-2}).

3.3 The influence of SOA on anthropogenic forcing

SOA particles have a strong potential to act as INPs and therefore influence the formation of cirrus clouds. We examined the radiative forcing of all anthropogenic aerosols on cirrus clouds when including the INPs from newly-nucleated SOA

particles. Figure 10 shows the column number concentration of INPs and zonal average of INPs from SOA in the PD and PI atmosphere. Changes in natural SOA precursors between the PI and PD atmospheres (i.e. isoprene, α-pinene and limonene emissions) are caused by changes in temperature as well as by changes in land-use, while changes in aromatic emissions are associated with anthropogenic emission growth. In addition, newly formed SOA particles grow to accumulation mode size as a result of coagulation of particles (sulfate and other newly formed SOA particles), deposition of gaseous sulfate and incorporation of other SOA compounds (e.g. through partitioning or kinetic uptake). Thus, the number concentration of INPs from SOA is much higher in the PD than that in the PI due to the much higher concentration of SOA in the accumulation mode in the PD (Zhu et al., 2019). The INPs from SOA are highest in the middle latitude of the NH in the PD, while the INPs from SOA are higher in the SH than that in the NH in the PI atmosphere (Figure 10a, 10b). The INPs from SOA in the PD are spread between 600hPa to 150hPa with a peak around 300hPa, so there is a possible influence on the formation of cirrus clouds (Figure 10b). The INPs from SOA in the PI have a peak concentration that is a little higher than those in the PD (Figure 10d). The global average *Ni* from heterogeneous nucleation increases by 1.86×10^{8} m^{-2} from PI to PD when including the INPs from SOA (Figure 11e), which is in contrast to the decrease in the global average *Ni* from heterogeneous nucleation in the case without SOA (Figure 5e). The INPs from SOA increase the *Ni* from heterogeneous nucleation in both the PD and PI cases when compared to the PD_Base and PI_ALL cases (Figure S5e, Figure S6e). However, the increase in *Ni* from heterogeneous nucleation in the PD is much larger than that in the PI because of the larger number concentration of INPs from SOA in the PD. As a result, the large increase in INPs from SOA between the PD and the PI enhances heterogeneous nucleation resulting in an increase in *Ni* from heterogeneous nucleation especially in the tropics around 150hPa and in

690 Antarctic from 400hPa to 200hPa (Figure 11f). The increase in the heterogeneous
691 nucleation when including SOA widely inhibits homogeneous nucleation in both the
692 PD and PI (Figure S5c, Figure S6c). In the PD, the increase in *Ni* from heterogeneous
693 nucleation even outweighs the decrease in *Ni* from homogeneous nucleation leading
694 to an increase of 0.4×10^8 m^{-2} in the global average *Ni* due to SOA compared to the
695 PD_Base case (Figure S5a). In contrast, the INPs from SOA in the PI case make a
696 larger contribution to the decrease in *Ni* from homogeneous nucleation than the
697 increase in *Ni* from heterogeneous nucleation resulting in a decrease in total *Ni* of -
698 0.31×10^8 m^{-2} compared to the PI_ALL case (Figure S6a). The inclusion of INPs
699 from SOA decreases *Ni* in the tropics but increases *Ni* in the mid to high latitudes in
700 both the NH and SH (Figure S5b, S6b). The global average *Ni* in the PD increases
701 while the global average *Ni* in the PI is decreased. Both changes are caused by
702 additional INPs from SOA (Figure S5a, S6a) resulting in a larger increase in the
703 global average *Ni* from the PI to PD compared to the case without SOA (compare
704 Figure 5a and Figure 11a). When including INPs from SOA, *Ni* increases to a large
705 extent over south Asia, the north Indian Ocean and Antarctica due to the increase in
706 heterogeneous nucleation, while *Ni* decreases over the mid to high latitude of East
707 Asia and the North Pacific Ocean (compare Figure 11a and Figure 5a).

708 The increased *Ni* leads to a significant increase in the IWP in south Asia, the
709 north Indian Ocean and Antarctica due to the reduction of gravitational removal,
710 while the IWP decreases significantly in the mid to high latitude of East Asia which
711 is caused by the decrease in *Ni* (Figure 11a). Compared with the case without SOA
712 (PD_Base-PI_ALL), the inclusion of SOA increases the difference in the IWP
713 between the PD and PI in Antarctica significantly because of the increase in *Ni* from
714 heterogeneous nucleation of INPs from SOA there (Figure 12a). The change in the
715 LWP due to dynamic feedbacks in the case with SOA is significant in only a few

716 grids, which is similar to the case without SOA (Figure 12c). The larger increases in
717 *Ni* and IWP over South Asia and the north Indian Ocean lead to the larger changes
718 in both SRF and LRF when including SOA compared to the case without SOA, while
719 the significant decrease in *Ni* in the mid to high latitudes over East Asia leads to a
720 significant decrease in the LRF. The increase in *Ni* and IWP in Antarctica only
721 increases the LRF but does not change the SRF because of the very low shortwave
722 flux in polar regions (Figure 12c, 12d). The larger decrease in the SRF offsets the
723 increase in the LRF in the tropics when including SOA resulting in a similar value
724 for NRF in the tropics for the cases with and without SOA (Figure 13f). However,
725 the more positive changes in the LRF from PI to PD in Antarctica and the Arctic
726 when including SOA explain the more positive NRF there compared to the case
727 without SOA (Figure 13f). In addition, the NRF in south Asia and north Africa
728 around 30ºN, where NRF is most positive in the case without SOA, becomes even
729 more positive when including SOA due to the larger increases in *Ni*. As a result, the
730 significant and larger positive NRF over Antarctica as well as south Asia and north
731 Africa around 30ºN cause an increase in the global average NRF due to all
732 anthropogenic aerosol to -0.04±0.08 W m^{-2} when including SOA compared to the
733 value of -0.20±0.05 W m^{-2} in the case without SOA. The NRF when including SOA
734 is up to 6.6 W m^{-2} in the Arabian Peninsula while it is as low as -4.8 W m^{-2} in the
735 north Indian Ocean (Figure 12g). Compared to the case without SOA, the global
736 average CRF is less negative (-0.14±0.07 W m^{-2} compared to -0.28 W m^{-2}) largely
737 due to the significant positive CRF over Antarctica (Figure 12f). Simultaneously,
738 the NRFC is more positive in the case with SOA than the case without SOA, which
739 offset 73% of the CRF (Figure 12e).
740

4. Conclusion and discussion

This work develops a new ice nucleation parameterization, HYBRID, which is a combination of the LP and KL parameterizations. The global model using this new scheme is able to simulate the growth and decay of ice particles in the updrafts and downdrafts associated with gravity waves as in the modified KL scheme (Penner et al., 2018), and is able to treat the changes in aerosol number concentration from freezing haze particles with fidelity in the sign of the change as in the LP scheme. The HYBRID scheme overcomes some of the deficiencies in previous ice nucleation schemes. We evaluated the HYBRID ice nucleation scheme by comparing the scheme with the Liu and Penner (2005) adiabatic parcel model and by comparing its global predictions using observed *Ni*. We used 10,000 parcel model simulations to show that the HYBRID box model predicts 7.3% larger *Ni* than the LP adiabatic parcel model with 21.5% larger *Ni* from homogeneous nucleation. The global model using the HYBRID scheme overestimates *Ni* between 195K and 215K somewhat compared to observations, as do earlier simulations with only the KL scheme (Penner et al., 2018). The results of *Ni* from the HYBRID scheme are in reasonable agreement with observations and thus were used in the CESM/IMPACT global model to estimate the radiative forcing of aerosols in large-scale cirrus clouds. The predicted *Ni* depends on the competition between homogeneous and heterogeneous nucleation. These two ice nucleation processes dominate the formation of *Ni* in different regions and altitudes. The global average *Ni* is dominated by homogeneous nucleation in the PD atmosphere.

We performed a series of model experiments using the HYBRID ice nucleation scheme to explore the forcing and cloud changes associated with changes in aircraft soot, sulfur emissions and all anthropogenic emissions from the PI to PD. Results are summarized in Table 3. The INPs from aircraft soot usually decrease *Ni* by the

767 inhibition of homogeneous nucleation in spite of some areas with small increases in
768 *Ni*. In contrast, the increase in sulfur emissions from PI to PD enhances
769 homogeneous nucleation in most regions and leads to a small decrease in the *Ni*
770 formed as a result of heterogeneous nucleation. We found that the effect of aerosols
771 in cirrus clouds could feedback to the meteorological state as determined by
772 temperature and RHi, which could have an opposite effect on the changes in *Ni* due
773 to either aircraft soot or sulfur emissions in the remote regions like the west Pacific
774 Ocean. These meteorological feedbacks partly reduce the changes in the global
775 average *Ni* due to anthropogenic emissions. The changes in *Ni* from PI to PD caused
776 by all anthropogenic emissions are dominated by the changes due to the sulfur
777 emissions, but the changes in surface and aircraft soot emission have some effects
778 on the inhibition of homogeneous nucleation.

779 The changes in *Ni* due to anthropogenic aerosols lead to changes in IWP as
780 well as LWP due to dynamical feedbacks. The changes in SRF and LRF are always
781 determined by the changes in the IWP (and *Ni*), but the changes in LWP could either
782 enhance or offset the effects of IWP on the radiative fluxes. Emissions of aircraft
783 soot lead to a positive change in the global average SRF while the global average
784 LRF is negative. The changes in sulfur emissions from the PI to PD atmosphere
785 leads to opposite changes in the global average SRF and LRF compared to aircraft
786 soot because of the different signs of changes in *Ni*. The total net forcing in cirrus
787 clouds is usually dominated by LRF but it is dominated by SRF when the changes
788 in warm clouds cause a feedback that reinforces the effect of cirrus clouds on
789 shortwave fluxes. As a result, the emission of aircraft soot has a negative global
790 average NRF of -0.14±0.07 W m^{-2} in large-scale cirrus clouds, while the changes in
791 the sulfur emissions from the PI to the PD lead to a small negative global average
792 NRF of -0.02±0.06 W m^{-2}. The global average NRF due to all anthropogenic
793 emissions from PI to PD, which is estimated to be -0.20±0.05 W m^{-2}, is dominated

by the NRF caused by increased sulfur emissions but is more negative than the forcing by sulfur emissions alone due to changes in the emissions of soot.

The influence of SOA on the anthropogenic forcing of aerosols in large-scale cirrus clouds was examined. The additional INPs from SOA increase the *Ni* from heterogeneous nucleation and decrease *Ni* from homogeneous nucleation, but the sign of the changes in the total *Ni* depends on the balance of these two effects. The high number concentration of INPs from SOA in the PD atmosphere causes an increase in *Ni* compared to not including INPs from SOA while the low number concentration in the PI atmosphere causes a decrease. As a result, the changes in *Ni* due to the changes in anthropogenic emissions from PI to PD are larger when including INPs from SOA than the case without SOA. The inclusion of SOA mainly increases the changes in the NRF in the polar regions and the regions around 30ºN, resulting in a less negative NRF of -0.04±0.07 W m^{-2} associated with the change in all anthropogenic emissions.

The radiative forcing of anthropogenic aerosols effect on cirrus clouds estimated in this study is less negative than the result indicated in Penner et al. (2009) (-0.38 to -0.56 W m^{-2}) and has a different sign compared with the result shown in Gettelman et al. (2012) (0.27±0.10 W m^{-2}). This is mostly caused by the different treatments for updraft velocity, the concentration of haze particles, and INPs as well as the application of a different ice nucleation scheme. Current models show that homogeneous nucleation dominates the formation of new ice particles in most regions over the world with the largest contribution to cirrus cloud formation in the tropical upper troposphere (Zhou et al., 2016; Shi and Liu, 2018; Shi et al., 2015). However, some observations indicated the importance and high occurrence frequency of heterogeneous nucleation in the tropical tropopause region (Jensen et al., 2013). Although the inclusion of INPs from newly formed SOA in this study inhibits homogeneous nucleation in the tropics, homogeneous nucleation is still

responsible for 75% of total *Ni* in the PD atmosphere. Laboratory measurements have supported other species acting as INP and enhancing heterogeneous nucleation such as solid ammonium sulfate (Abbatt et al., 2006), which has not been considered in current global climate models. Additional INPs from anthropogenic ammonium sulfate can be expected to increase the anthropogenic forcing in cirrus clouds to be less negative and possibly even positive. The HYBRID ice nucleation scheme overestimates somewhat the ice number concentration produced from homogeneous nucleation compared to a full parcel model. An explicit representation of the ice nucleation process used in the global climate model may be helpful to predict the ice number and therefore radiation budget more correctly in the future. The ability of SOA to act as an INP probably varies depends on the property of different SOA compounds as well as their particle size and mixing state (Baustian et al., 2013; Berkemeier et al., 2014; Charnawskas et al., 2017; Shiraiwa et al., 2017). A global climate model coupled online with the formation mechanism of SOA together with an increased understanding of the ability of SOA to act as an INP would help in estimating the contribution of SOA to ice particle formation more accurately.

Code and data availability

The latest version of CESM/IMPACT model and data used in this study are available from the corresponding authors upon request.

Author contribution

JZ developed the model, performed the simulations, analyzed all data. JP guided the model development and data analysis. Both authors contributed to writing the paper.

Competing interests

The authors declare that they have no conflict of interest.

Acknowledgments

We are grateful to the reviewers and for funding from NSF-GEO grant number 1540954 and National Natural Science Foundation of China (Grant 41625014). Computer time was provided by the NCAR CISL.

References

Abbatt, J., Benz, S., Cziczo, D., Kanji, Z., Lohmann, U., and Möhler, O.: Solid ammonium sulfate aerosols as ice nuclei: A pathway for cirrus cloud formation, Science, 313, 1770-1773, 2006.

Andreae, M. O., Afchine, A., Albrecht, R., Holanda, B. A., Artaxo, P., Barbosa, H. M. J., Borrmann, S., Cecchini, M. A., Costa, A., Dollner, M., Fütterer, D., Järvinen, E., Jurkat, T., Klimach, T., Konemann, T., Knote, C., Krämer, M., Krisna, T., Machado, L. A. T., Mertes, S., Minikin, A., Pöhlker, C., Pöhlker, M. L., Pöschl, U., Rosenfeld, D., Sauer, D., Schlager, H., Schnaiter, M., Schneider, J., Schulz, C., Spanu, A., Sperling, V. B., Voigt, C., Walser, A., Wang, J., Weinzierl, B., Wendisch, M., and Ziereis, H.: Aerosol characteristics and particle production in the upper troposphere over the Amazon Basin, Atmospheric Chemistry and Physics, 18, 921-961, 10.5194/acp-18-921-2018, 2018.

Barahona, D., and Nenes, A.: Parameterization of cirrus cloud formation in large-scale models: Homogeneous nucleation, Journal of Geophysical Research: Atmospheres, 113, 2008.

Barrett, S., Prather, M., Penner, J., Selkirk, H., Balasubramanian, S., Dopelheuer, A., Fleming, G., Gupta, M., Halthore, R., and Hileman, J.: Guidance on the use of AEDT gridded aircraft emissions in atmospheric models, A technical note submitted to the US Federal Aviation Administration, Massachusetts Institute of Technology (MIT), 2010.

Baustian, K. J., Wise, M. E., Jensen, E. J., Schill, G. P., Freedman, M. A., and Tolbert, M. A.: State transformations and ice nucleation in amorphous (semi-)solid organic aerosol, Atmospheric Chemistry and Physics, 13, 5615-5628, 10.5194/acp-13-5615-2013, 2013.

Berkemeier, T., Shiraiwa, M., Pöschl, U., and Koop, T.: Competition between water uptake and ice nucleation by glassy organic aerosol particles, Atmospheric Chemistry and Physics, 14, 12513-12531, 10.5194/acp-14-12513-2014, 2014.

Boville, B. A., P. J. Rasch, J. J. Hack, and J. R. McCaa: Representation of clouds and precipitation processes in the Community Atmosphere Model version 3 (CAM3). J. Climate, 19, 2184–2198, 2006.

Cantrell, W., and Heymsfield, A.: Production of ice in tropospheric clouds: A review, Bulletin of the American Meteorological Society, 86, 795-808, 2005.

Charnawskas, J. C., Alpert, P. A., Lambe, A. T., Berkemeier, T., O'Brien, R. E., Massoli, P., Onasch, T. B., Shiraiwa, M., Moffet, R. C., Gilles, M. K., Davidovits, P., Worsnop, D. R., and Knopf, D. A.: Condensed-phase biogenic-anthropogenic interactions with implications for cold cloud formation, Faraday Discuss, 200, 165-194, 10.1039/c7fd00010c, 2017.

Cziczo, D. J., Murphy, D. M., Hudson, P. K., and Thomson, D. S.: Single particle measurements of the chemical composition of cirrus ice residue during CRYSTAL-FACE, Journal of Geophysical Research-Atmospheres, 109, 10.1029/2003jd004032, 2004.Cziczo, D. J., Froyd, K. D., Hoose, C., Jensen, E. J., Diao, M., Zondlo, M. A., Smith, J. B., Twohy, C. H., and Murphy, D. M.: Clarifying the dominant sources and mechanisms of cirrus cloud formation, Science, 340, 1320-1324, 2013.

DeMott, P., Cziczo, D., Prenni, A., Murphy, D., Kreidenweis, S., Thomson, D., Borys, R., and Rogers, D.: Measurements of the concentration and composition of nuclei for cirrus formation, Proceedings of the National Academy of Sciences, 100, 14655-14660, 2003.

Fan, J., Wang, Y., Rosenfeld, D., and Liu, X.: Review of aerosol–cloud interactions: Mechanisms, significance, and challenges, Journal of the Atmospheric Sciences, 73, 4221-4252, 2016.

Gary, B. L.: Mesoscale temperature fluctuations in the stratosphere, Atmospheric Chemistry and Physics, 6, 4577-4589, 2006.

Gary, B. L.: Mesoscale temperature fluctuations in the Southern Hemisphere stratosphere, Atmospheric Chemistry and Physics, 8, 4677-4681, 2008.

Gettelman, A., Liu, X., Barahona, D., Lohmann, U., and Chen, C.: Climate impacts of ice nucleation, Journal of Geophysical Research: Atmospheres, 117, 10.1029/2012jd017950, 2012.

Gordon, H., Sengupta, K., Rap, A., Duplissy, J., Frege, C., Williamson, C., Heinritzi, M., Simon, M., Yan, C., Almeida, J., Trostl, J., Nieminen, T., Ortega, I. K., Wagner, R., Dunne, E. M., Adamov, A., Amorim, A., Bernhammer, A. K., Bianchi, F., Breitenlechner, M., Brilke, S., Chen, X., Craven, J. S., Dias, A., Ehrhart, S., Fischer, L., Flagan, R. C., Franchin, A., Fuchs, C., Guida, R., Hakala, J., Hoyle, C. R., Jokinen, T., Junninen, H., Kangasluoma, J., Kim, J., Kirkby, J., Krapf, M., Kurten, A., Laaksonen, A., Lehtipalo, K., Makhmutov, V., Mathot, S., Molteni, U., Monks, S. A., Onnela, A., Perakyla, O., Piel, F., Petaja, T., Praplan, A. P., Pringle, K. J., Richards, N. A., Rissanen, M. P., Rondo, L., Sarnela, N., Schobesberger, S., Scott, C. E., Seinfeld, J. H., Sharma, S., Sipila, M., Steiner, G., Stozhkov, Y., Stratmann,

F., Tome, A., Virtanen, A., Vogel, A. L., Wagner, A. C., Wagner, P. E., Weingartner, E., Wimmer, D., Winkler, P. M., Ye, P., Zhang, X., Hansel, A., Dommen, J., Donahue, N. M., Worsnop, D. R., Baltensperger, U., Kulmala, M., Curtius, J., and Carslaw, K. S.: Reduced anthropogenic aerosol radiative forcing caused by biogenic new particle formation, Proc Natl Acad Sci U S A, 113, 12053-12058, 10.1073/pnas.1602360113, 2016.

Hendricks, J., Kärcher, B., and Lohmann, U.: Effects of ice nuclei on cirrus clouds in a global climate model, Journal of Geophysical Research, 116, 10.1029/2010jd015302, 2011.

Hoesly, R. M., Smith, S. J., Feng, L., Klimont, Z., Janssens-Maenhout, G., Pitkanen, T., Seibert, J. J., Vu, L., Andres, R. J., and Bolt, R. M.: Historical (1750–2014) anthropogenic emissions of reactive gases and aerosols from the Community Emissions Data System (CEDS), Geoscientific Model Development (Online), 11, 2018.

Hong, Y., Liu, G. and Li, J. L.: Assessing the radiative effects of global ice clouds based on CloudSat and CALIPSO measurements. Journal of Climate, 29(21), 7651-7674, 2016.

Hoose, C., and Möhler, O.: Heterogeneous ice nucleation on atmospheric aerosols: a review of results from laboratory experiments, Atmospheric Chemistry and Physics, 12, 9817-9854, 10.5194/acp-12-9817-2012, 2012.

Ignatius, K., Kristensen, T. B., Jarvinen, E., Nichman, L., Fuchs, C., Gordon, H., Herenz, P., Hoyle, C. R., Duplissy, J., Garimella, S., Dias, A., Frege, C., Hoppel, N., Troestl, J., Wagner, R., Yan, C., Amorim, A., Baltensperger, U., Curtius, J., Donahue, N. M., Gallagher, M. W., Kirkby, J., Kulmala, M., Mohler, O., Saathoff, H., Schnaiter, M., Tome, A., Virtanen, A., Worsnop, D., and Stratmann, F.: Heterogeneous ice nucleation of viscous secondary organic aerosol produced from ozonolysis of alpha-pinene, Atmospheric Chemistry and Physics, 16, 6495-6509, 10.5194/acp-16-6495-2016, 2016.

IPCC: Climate Change 2013: The Physical Science Basis. Contribution of Working Group I to the Fifth Assessment Report of the Intergovernmental Panel on Climate Change, Cambridge University Press, Cambridge, United Kingdom and New York, NY, USA, 1535 pp., 2013.

Jensen, E. J., Diskin, G., Lawson, R. P., Lance, S., Bui, T. P., Hlavka, D., McGill, M., Pfister, L., Toon, O. B., and Gao, R.: Ice nucleation and dehydration in the

Tropical Tropopause Layer, Proc Natl Acad Sci U S A, 110, 2041-2046, 10.1073/pnas.1217104110, 2013.

Kärcher, B., Hendricks, J., and Lohmann, U.: Physically based parameterization of cirrus cloud formation for use in global atmospheric models, Journal of Geophysical Research, 111, 10.1029/2005jd006219, 2006.

Kärcher, B., and Lohmann, U.: A parameterization of cirrus cloud formation: Homogeneous freezing of supercooled aerosols, Journal of Geophysical Research: Atmospheres, 107, AAC 4-1-AAC 4-10, 2002.

Knopf, D. A., Alpert, P. A., and Wang, B.: The Role of Organic Aerosol in Atmospheric Ice Nucleation: A Review, ACS Earth and Space Chemistry, 2, 168-202, 10.1021/acsearthspacechem.7b00120, 2018.

Koehler, K. A., DeMott, P. J., Kreidenweis, S. M., Popovicheva, O. B., Petters, M. D., Carrico, C. M., Kireeva, E. D., Khokhlova, T. D., and Shonija, N. K.: Cloud condensation nuclei and ice nucleation activity of hydrophobic and hydrophilic soot particles, Physical Chemistry Chemical Physics, 11, 7906-7920, 2009.

Koop, T., Luo, B. P., Tsias, A., and Peter, T.: Water activity as the determinant for homogeneous ice nucleation in aqueous solutions, Nature, 406, 611-614, 10.1038/35020537, 2000.

Koop, T., Bookhold, J., Shiraiwa, M., and Poschl, U.: Glass transition and phase state of organic compounds: dependency on molecular properties and implications for secondary organic aerosols in the atmosphere, Phys Chem Chem Phys, 13, 19238-19255, 10.1039/c1cp22617g, 2011.

Krämer, M., Schiller, C., Afchine, A., Bauer, R., Gensch, I., Mangold, A., Schlicht, S., Spelten, N., Sitnikov, N., and Borrmann, S.: Ice supersaturations and cirrus cloud crystal numbers, Atmospheric Chemistry and Physics, 9, 3505-3522, 2009.

Krämer, M., Rolf, C., Luebke, A., Afchine, A., Spelten, N., Costa, A., Meyer, J., Zoeger, M., Smith, J., and Herman, R. L.: A microphysics guide to cirrus clouds-Part 1: Cirrus types, Atmospheric Chemistry and Physics, 16, 3463-3483, 2016.

Krämer, M., C. Rolf, N. Spelten, A. Afchine, D. Fahey, E. Jensen, S. Khaykin, T. Kuhn, P. Lawson, and A. Lykov: A Microphysics Guide to Cirrus–Part II: Climatologies of Clouds and Humidity from Observations, *Atmospheric Chemistry and Physics Discussions*, doi:10.5194/acp-2020-40, 2020.

Kuebbeler, M., Lohmann, U., Hendricks, J., and Kärcher, B.: Dust ice nuclei effects on cirrus clouds, Atmos. Chem. Phys, 14, 3027-3046, 2014.

Kristjánsson, J. E., J. M. Edwards, and D. L. Mitchell: Impact of a new scheme for optical properties of ice crystals on climates of two gems. J. Geophys. Res., 105, 10 063–10 079, 2000.

Li, J. L. F., Waliser, D. E., Chen, W. T., Guan, B., Kubar, T., Stephens, G., Ma, H. Y., Deng, M., Donner, L., Seman, C., and Horowitz, L.: An observationally based evaluation of cloud ice water in CMIP3 and CMIP5 GCMs and contemporary reanalyses using contemporary satellite data, Journal of Geophysical Research-Atmospheres, 117, 10.1029/2012jd017640, 2012.

Liu, X., and Penner, J. E.: Ice nucleation parameterization for global models, Meteorologische Zeitschrift, 14, 499-514, 2005.Liu, X., Easter, R. C., Ghan, S. J., Zaveri, R., Rasch, P., Shi, X., Lamarque, J. F., Gettelman, A., Morrison, H., Vitt, F., Conley, A., Park, S., Neale, R., Hannay, C., Ekman, A. M. L., Hess, P., Mahowald, N., Collins, W., Iacono, M. J., Bretherton, C. S., Flanner, M. G., and Mitchell, D.: Toward a minimal representation of aerosols in climate models: description and evaluation in the Community Atmosphere Model CAM5, Geoscientific Model Development, 5, 709-739, 10.5194/gmd-5-709-2012, 2012.

Liu, X., Penner, J. E., and Herzog, M.: Global modeling of aerosol dynamics: Model description, evaluation, and interactions between sulfate and nonsulfate aerosols, Journal of Geophysical Research: Atmospheres, 110, 2005.Liu, X., and Shi, X.: Sensitivity of homogeneous ice nucleation to aerosol perturbations and its implications for aerosol indirect effects through cirrus clouds, Geophysical Research Letters, 45, 1684-1691, 2018.

Lohmann, U., von Salzen, K., McFarlane, N., Leighton, H. G., and Feichter, J.: Tropospheric sulfur cycle in the Canadian general circulation model, Journal of Geophysical Research: Atmospheres, 104, 26833-26858, 1999.

Lohmann, U.: Possible aerosol effects on ice clouds via contact nucleation, Journal of the atmospheric sciences, 59, 647-656, 2002.

Mahrt, F., Kilchhofer, K., Marcolli, C., Grönquist, P., David, R. O., Rösch, M., Lohmann, U., and Kanji, Z. A.: The Impact of Cloud Processing on the Ice Nucleation Abilities of Soot Particles at Cirrus Temperatures, Journal of Geophysical Research: Atmospheres, 2019.

Matus, A. V. and L'Ecuyer, T. S. : The role of cloud phase in Earth's radiation budget. Journal of Geophysical Research: Atmospheres, 122(5), 2559-2578, 2017.

Pajunoja, A., Malila, J., Hao, L. Q., Joutsensaari, J., Lehtinen, K. E. J., and Virtanen, A.: Estimating the Viscosity Range of SOA Particles Based on Their Coalescence Time, Aerosol Sci. Technol., 48, I-IV, 10.1080/02786826.2013.870325, 2014.

Penner, J. E., Chen, Y., Wang, M., and Liu, X.: Possible influence of anthropogenic aerosols on cirrus clouds and anthropogenic forcing, Atmospheric Chemistry and Physics, 9, 879-896, 2009.

Penner, J. E., Zhou, C., Garnier, A., and Mitchell, D. L.: Anthropogenic Aerosol Indirect Effects in Cirrus Clouds, Journal of Geophysical Research: Atmospheres, 123, 11,652-611,677, 10.1029/2018jd029204, 2018.

Podglajen, A., Hertzog, A., Plougonven, R., and Legras, B.: Lagrangian temperature and vertical velocity fluctuations due to gravity waves in the lower stratosphere, Geophysical Research Letters, 43, 3543-3553, 2016.

Pratt, K., Murphy, S., Subramanian, R., DeMott, P., Kok, G., Campos, T., Rogers, D., Prenni, A., Heymsfield, A., and Seinfeld, J.: Flight-based chemical characterization of biomass burning aerosols within two prescribed burn smoke plumes, Atmospheric Chemistry and Physics, 11, 12549-12565, 2011.

Prenni, A. J., DeMott, P. J., Sullivan, A. P., Sullivan, R. C., Kreidenweis, S. M., and Rogers, D. C.: Biomass burning as a potential source for atmospheric ice nuclei: Western wildfires and prescribed burns, Geophysical Research Letters, 39, 2012.

Renbaum-Wolff, L., Grayson, J. W., Bateman, A. P., Kuwata, M., Sellier, M., Murray, B. J., Shilling, J. E., Martin, S. T., and Bertram, A. K.: Viscosity of alpha-pinene secondary organic material and implications for particle growth and reactivity, Proc. Natl. Acad. Sci. U. S. A., 110, 8014-8019, 10.1073/pnas.1219548110, 2013.

Richardson, M. S., DeMott, P. J., Kreidenweis, S. M., Cziczo, D. J., Dunlea, E. J., Jimenez, J. L., Thomson, D. S., Ashbaugh, L. L., Borys, R. D., Westphal, D. L., Casuccio, G. S., and Lersch, T. L.: Measurements of heterogeneous ice nuclei in the western United States in springtime and their relation to aerosol characteristics, Journal of Geophysical Research-Atmospheres, 112, 10.1029/2006jd007500, 2007.

Saukko, E., Lambe, A. T., Massoli, P., Koop, T., Wright, J. P., Croasdale, D. R., Pedernera, D. A., Onasch, T. B., Laaksonen, A., Davidovits, P., Worsnop, D. R., and

Virtanen, A.: Humidity-dependent phase state of SOA particles from biogenic and anthropogenic precursors, Atmospheric Chemistry and Physics, 12, 7517-7529, 10.5194/acp-12-7517-2012, 2012.

Shi, X., Liu, X., and Zhang, K.: Effects of pre-existing ice crystals on cirrus clouds and comparison between different ice nucleation parameterizations with the Community Atmosphere Model (CAM5), Atmospheric Chemistry and Physics, 15, 1503-1520, 10.5194/acp-15-1503-2015, 2015.

Shi, X., and Liu, X.: Sensitivity Study of Anthropogenic Aerosol Indirect Forcing through Cirrus Clouds with CAM5 Using Three Ice Nucleation Parameterizations, Journal of Meteorological Research, 32, 693-706, 10.1007/s13351-018-8011-z, 2018.

Shiraiwa, M., Li, Y., Tsimpidi, A. P., Karydis, V. A., Berkemeier, T., Pandis, S. N., Lelieveld, J., Koop, T., and Pöschl, U.: Global distribution of particle phase state in atmospheric secondary organic aerosols, Nature Communications, 8, 15002, 10.1038/ncomms15002, 2017.

Storelvmo, T.: Aerosol Effects on Climate via Mixed-Phase and Ice Clouds, Annual Review of Earth and Planetary Sciences, 45, 199-222, 10.1146/annurev-earth-060115-012240, 2017.

Tilmes, S., Lamarque, J.-F., Emmons, L. K., Kinnison, D. E., Marsh, D., Garcia, R. R., Smith, A. K., Neely, R. R., Conley, A., Vitt, F., Val Martin, M., Tanimoto, H., Simpson, I., Blake, D. R., and Blake, N.: Representation of the Community Earth System Model (CESM1) CAM4-chem within the Chemistry-Climate Model Initiative (CCMI), Geoscientific Model Development, 9, 1853-1890, 10.5194/gmd-9-1853-2016, 2016.

van Marle, M. J. E., Kloster, S., Magi, B. I., Marlon, J. R., Daniau, A.-L., Field, R. D., Arneth, A., Forrest, M., Hantson, S., Kehrwald, N. M., Knorr, W., Lasslop, G., Li, F., Mangeon, S., Yue, C., Kaiser, J. W., and van der Werf, G. R.: Historic global biomass burning emissions for CMIP6 (BB4CMIP) based on merging satellite observations with proxies and fire models (1750–2015), Geoscientific Model Development, 10, 3329-3357, 10.5194/gmd-10-3329-2017, 2017.

Wagner, R., Höhler, K., Huang, W., Kiselev, A., Möhler, O., Mohr, C., Pajunoja, A., Saathoff, H., Schiebel, T., Shen, X., and Virtanen, A.: Heterogeneous ice nucleation of α-pinene SOA particles before and after ice cloud processing, Journal of Geophysical Research: Atmospheres, 122, 4924-4943, 10.1002/2016jd026401, 2017.

Waliser, D. E., Li, J. L. F., Woods, C. P., Austin, R. T., Bacmeister, J., Chern, J., Del Genio, A., Jiang, J. H., Kuang, Z., and Meng, H.: Cloud ice: A climate model challenge with signs and expectations of progress, Journal of Geophysical Research: Atmospheres, 114, 2009.

Wang, B., Lambe, A. T., Massoli, P., Onasch, T. B., Davidovits, P., Worsnop, D. R., and Knopf, D. A.: The deposition ice nucleation and immersion freezing potential of amorphous secondary organic aerosol: Pathways for ice and mixed-phase cloud formation, Journal of Geophysical Research: Atmospheres, 117, 2012.

Wang, M., Liu, X., Zhang, K., and Comstock, J. M.: Aerosol effects on cirrus through ice nucleation in the Community Atmosphere Model CAM5 with a statistical cirrus scheme, Journal of Advances in Modeling Earth Systems, 6, 756-776, 10.1002/2014ms000339, 2014.Wang, M., and Penner, J. E.: Aerosol indirect forcing in a global model with particle nucleation, Atmospheric Chemistry and Physics, 9, 239-260, 2009.

Wang, M., and Penner, J. E.: Cirrus clouds in a global climate model with a statistical cirrus cloud scheme, Atmospheric Chemistry and Physics, 10, 5449-5474, 10.5194/acp-10-5449-2010, 2010.

Wang, P. H., Minnis, P., McCormick, M. P., Kent, G. S., and Skeens, K. M.: A 6-year climatology of cloud occurrence frequency from Stratospheric Aerosol and Gas Experiment II observations (1985 – 1990), Journal of Geophysical Research: Atmospheres, 101, 29407-29429, 1996.

Wilson, T. W., Murray, B. J., Wagner, R., Möhler, O., Saathoff, H., Schnaiter, M., Skrotzki, J., Price, H. C., Malkin, T. L., Dobbie, S., and Al-Jumur, S. M. R. K.: Glassy aerosols with a range of compositions nucleate ice heterogeneously at cirrus temperatures, Atmospheric Chemistry and Physics, 12, 8611-8632, 10.5194/acp-12-8611-2012, 2012.

Wilkerson, J. T., Jacobson, M. Z., Malwitz, A., Balasubramanian, S., Wayson, R., Fleming, G., Naiman, A. D., and Lele, S. K.: Analysis of emission data from global commercial aviation: 2004 and 2006, Atmos. Chem. Phys., 10, 6391–6408, https://doi.org/10.5194/acp-10-6391-2010, 2010.

Yun, Y., Penner, J. E., and Popovicheva, O.: The effects of hygroscopicity on ice nucleation of fossil fuel combustion aerosols in mixed-phase clouds, Atmospheric Chemistry and Physics, 13, 4339-4348, 10.5194/acp-13-4339-2013, 2013.

Zender, C. S., Bian, H., and Newman, D.: Mineral Dust Entrainment and Deposition (DEAD) model: Description and 1990s dust climatology, Journal of Geophysical Research: Atmospheres, 108, 2003.

Zhang, K., Wan, H., Liu, X., Ghan, S. J., Kooperman, G. J., Ma, P.-L., Rasch, P. J., Neubauer, D., and Lohmann, U.: On the use of nudging for aerosol–climate model intercomparison studies, Atmospheric Chemistry and Physics, 14, 8631-8645, 2014.

Zhou, C., and Penner, J. E.: Aircraft soot indirect effect on large-scale cirrus clouds: Is the indirect forcing by aircraft soot positive or negative?, Journal of Geophysical Research-Atmospheres, 119, 11303-11320, 10.1002/2014jd021914, 2014.

Zhou, C., Penner, J. E., Lin, G., Liu, X., and Wang, M.: What controls the low ice number concentration in the upper troposphere?, Atmospheric Chemistry and Physics, 16, 12411-12424, 10.5194/acp-16-12411-2016, 2016.

Zhu, J., and Penner, J. E.: Global Modeling of Secondary Organic Aerosol With Organic Nucleation, Journal of Geophysical Research: Atmospheres, 124, 8260-8286, 2019.

Zhu, J., and Penner, J. E.: Indirect effects of secondary organic aerosol on cirrus clouds, Journal of Geophysical Research: Atmospheres,10.1029/2019JD032233, 2020.

Zhu, J., Penner, J. E., Lin, G., Zhou, C., Xu, L., and Zhuang, B.: Mechanism of SOA formation determines magnitude of radiative effects, Proc Natl Acad Sci U S A, 114, 12685-12690, 10.1073/pnas.1712273114, 2017.

Zhu, J., Penner, J. E., Yu, F., Sillman, S., Andreae, M. O., and Coe, H.: Decrease in radiative forcing by organic aerosol nucleation, climate, and land use change, Nature Communications, 10, 423, 10.1038/s41467-019-08407-7, 2019.

Tables

Table 1. Summary of assumptions for aerosols to be effective INPs in the model

Aerosol component	Assumption to be effective INPs
Fossil/bio-fuel OM/BC	0.05% of fSootwith <1 monolayers of sulfate and 0.1% with 1-3 monolayers of sulfate when RHi reaches 120%
Biomass OM/BC	0.1% of bSoot when RHi reaches 120%
Aircraft OM/BC	Pre-activated aircraft soot within contrails with less than 3 monolayers of sulfate when RHi reaches 120%
Dust	Dust with fewer than 3 monolayers of sulfate coating when RHi reaches 120%
SOA	The newly formed SOA grow to the accumulation mode and meets the requirements of the glass transition temperature and RHi calculated using the equations in Wang et al. (2012) when RHi reaches 120%

1153 Table 2. Description of cases

Case name	Description
PD_Base	Emissions for the present day (≈2000) for anthropogenic sulfur, surface and aircraft soot
PI_cSoot	As in PD_Base without INPs from pre-activated aircraft soot in contrails
PI_SO4	As in PD_Base, but with the anthropogenic sulfur emission for the preindustrial period (≈1750)
PI_ALL	As in PD_Base, but with the anthropogenic sulfur emission and surface soot emission for the pre-industrial period (≈1750) and without aircraft soot
PD_SOA	As in PD_Base, but adding INPs from newly formed SOA particles in present day
PI_SOA	As in PI_ALL, but adding INPs from newly formed SOA particles in preindustrial period

1154 Note: SOA=secondary organic aerosol; INP=ice nucleating particle.

1155

1156 Table 3. Forcing and cloud changes associated with changes in aircraft soot, sulfur
1157 and all anthropogenic aerosols.

Parameter	PD_Base-PI_cSoot	PD_Base-PI_SO4	PD_Base-PI_ALL	PD_SOA-PI_SOA
Ni (10^7 m^{-2})	-1.00±2.40	7.26±2.88	4.93±1.80	11.96±2.29
IWP (g m^{-2})	-0.13±0.06	0.07±0.06	-0.13±0.04	-0.12±0.05
LWP (g m^{-2})	-0.19±0.04	0.16±0.07	-0.05±0.08	0.03±0.06
FSNT (W m^{-2})	0.35±0.13	-0.36±0.10	0.10±0.06	-0.14±0.11
FLNT (W m^{-2})	-0.49±0.09	0.33±0.05	-0.30±0.06	0.10±0.04
FNT (W m^{-2})	-0.14±0.07	-0.02±0.06	-0.20±0.05	-0.04±0.08

1158

1159

Figures

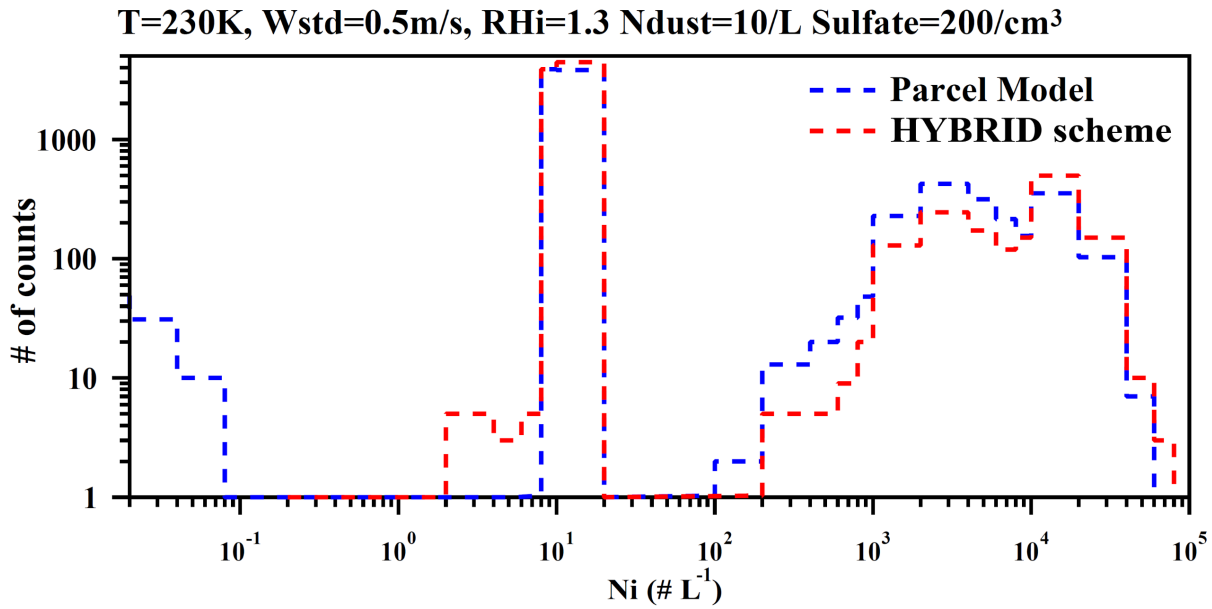

Figure 1. Histogram of predicted ice number concentration for 10,000 simulations using an adiabatic parcel model (blue dashed line) and a box model using the HYBRID scheme (red dashed line). Wstd is the standard deviation of the assumed pdf of updraft velocities, while Ndust and Sulfate are the assumed dust and sulfate number concentrations.

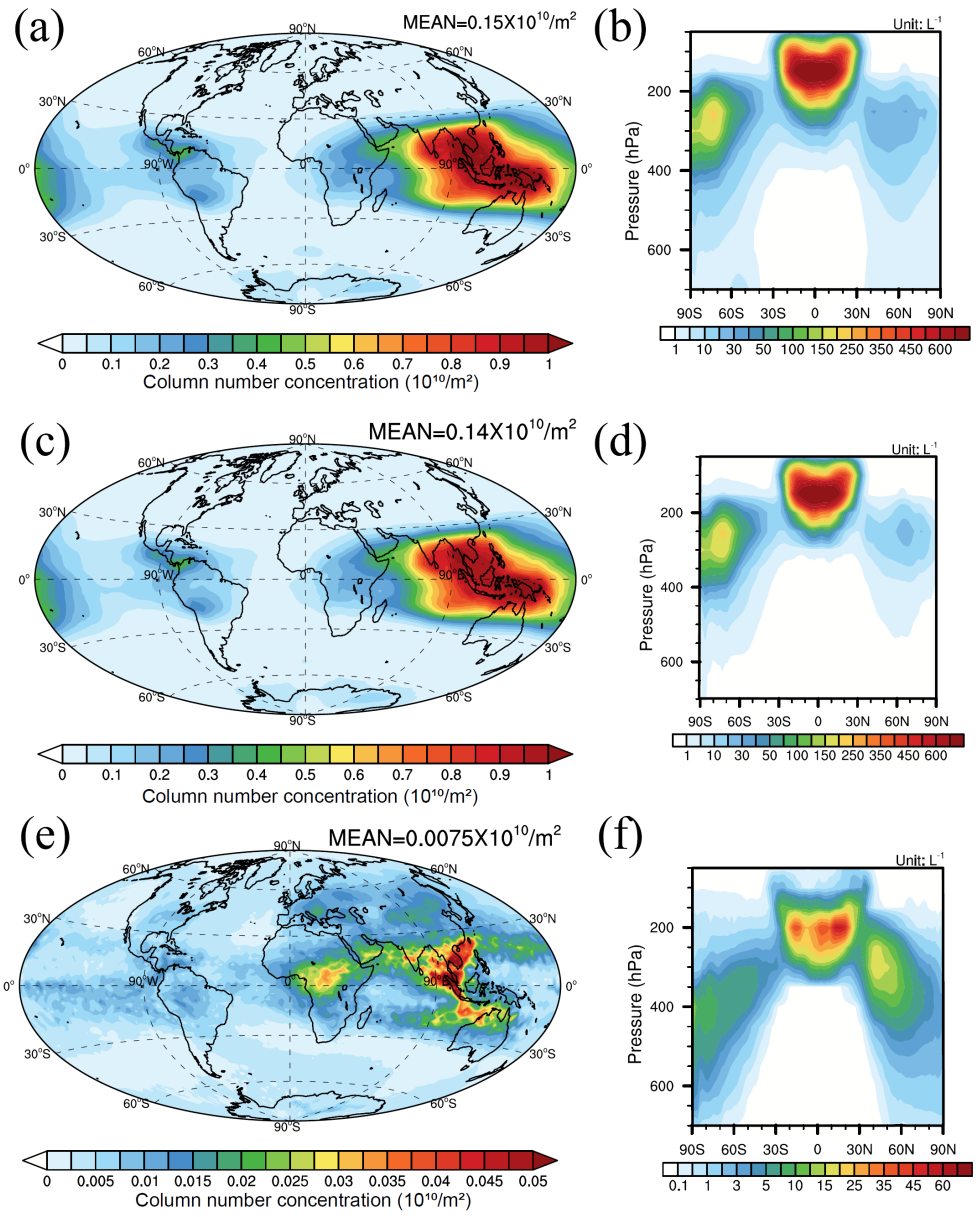

Figure 2. The vertically integrated total Ni in PD_Base case (a), Ni from homogeneous nucleation (c) and Ni from heterogeneous nucleation (e). The zonal average plots of Ni in PD_Base case (b), Ni from homogeneous nucleation (d) and Ni from heterogeneous nucleation (f). Note: the vertical axis in (b), (d) and (f) are in hybrid pressure levels

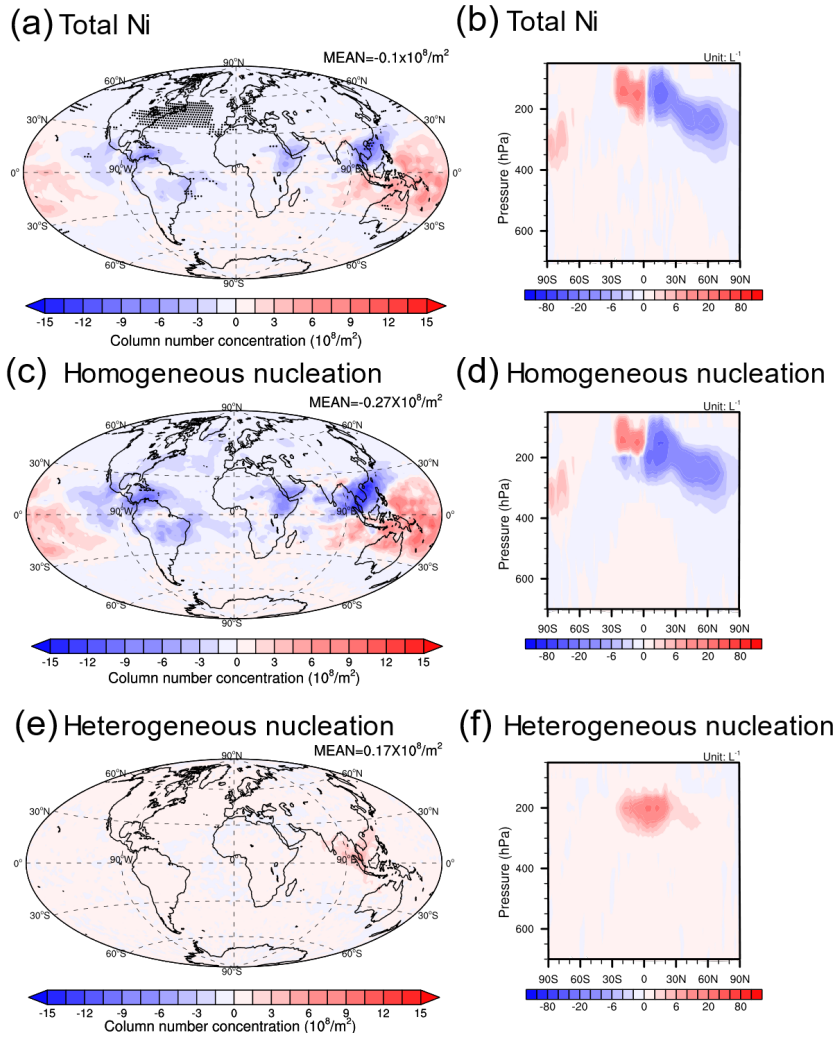

Figure 3. The annual average change in column number concentration (a, c, e) and zonal average number concentration (b, d, f) of total ice (a, b), ice from homogeneous nucleation (c, d) and ice from heterogeneous nucleation (e, f) for the difference between the PD_Base and PI_cSoot cases. Differences significant at the 90% level according to a Student's t test are depicted by points in (a).

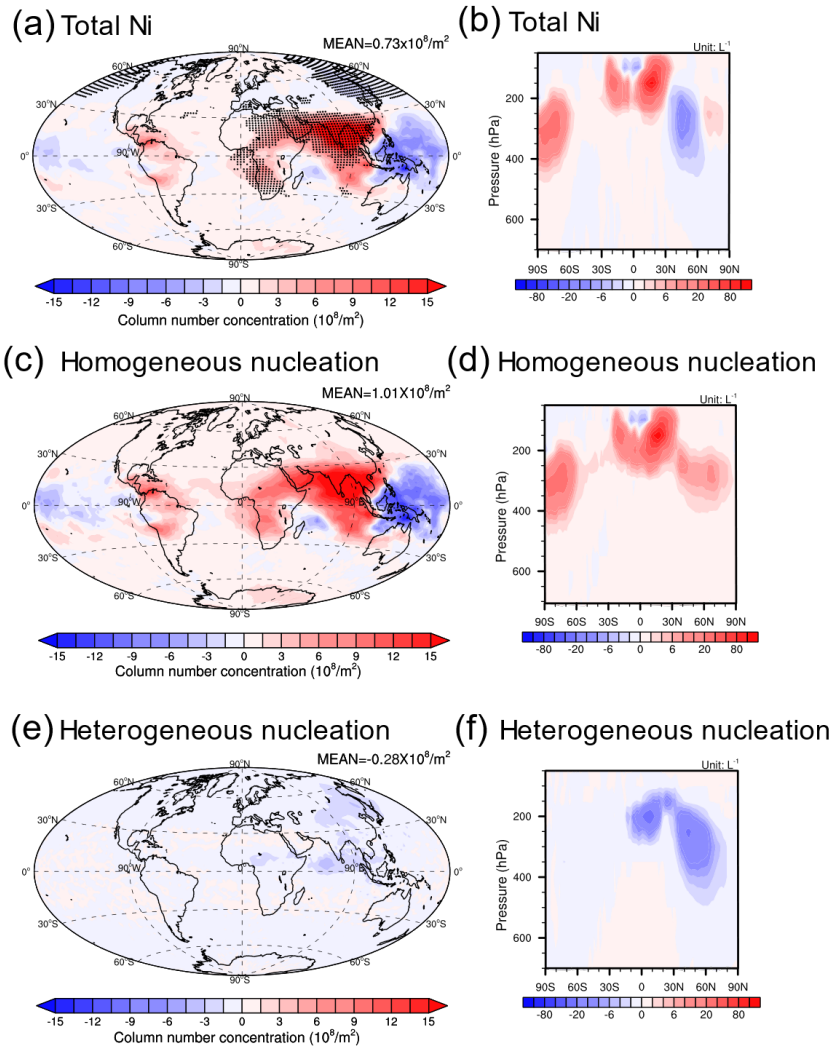

1184

1185 Figure 4. As in Figure 3 but for the difference between the PD_Base and PI_SO4

1186 cases. Differences significant at the 90% level according to a Student's t test are

1187 depicted by points in (a).

1188

1189

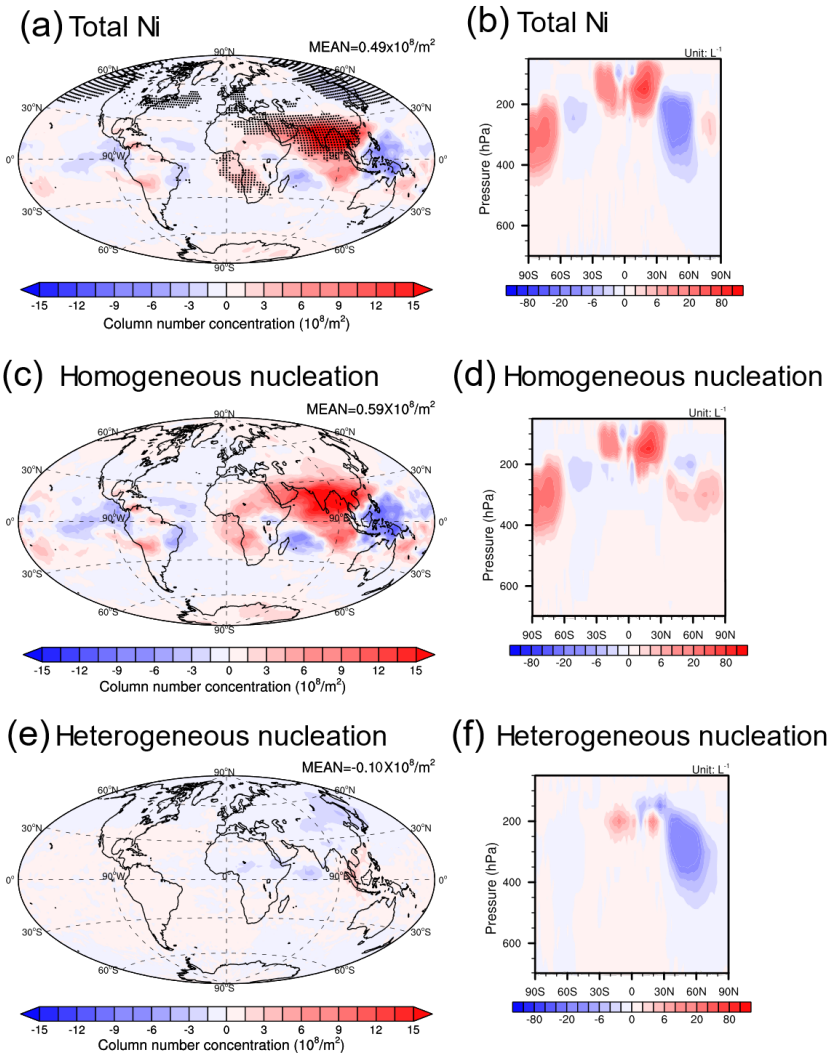

1190

1191 Figure 5. As in Figure 3 but for the difference between the PD_Base and PI_ALL

1192 cases. Differences significant at the 90% level according to a Student's t test are

1193 depicted by points in (a).

1194

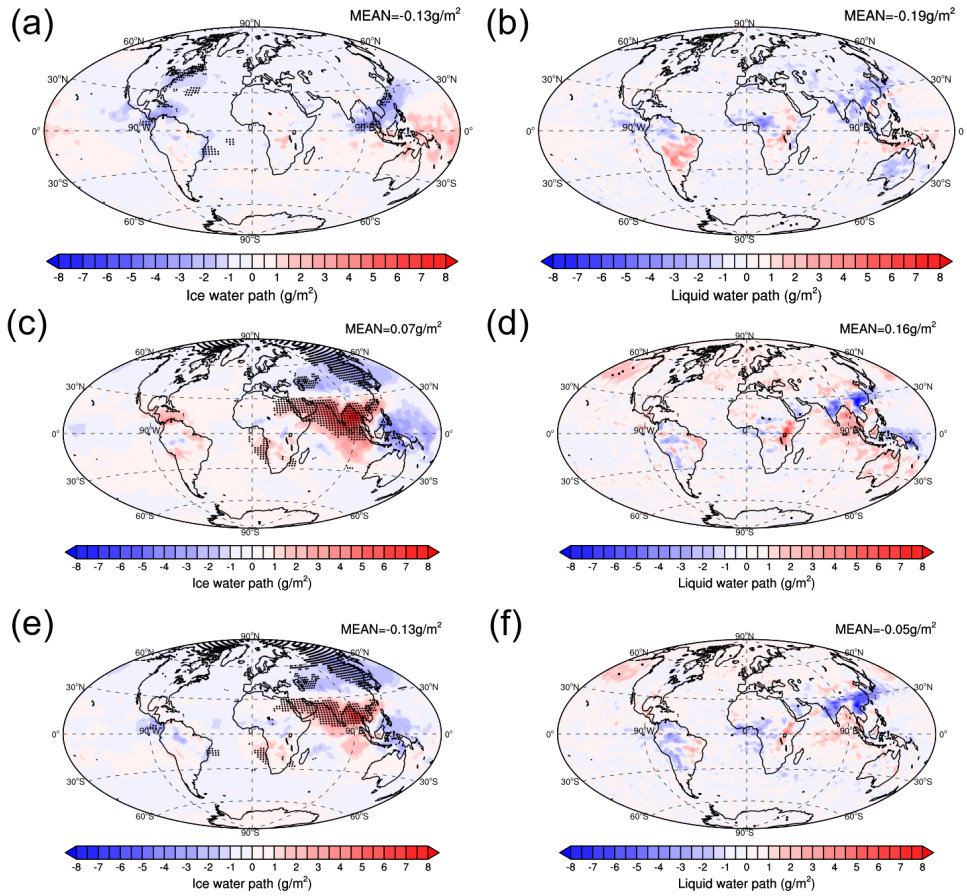

Figure 6. Annual mean plots of the change in vertically integrated averaged ice water path (a, c, e) and liquid water path (b, d, f) for the difference between the PD_Base and PI_cSoot cases (a, b), PD_Base and PI_SO4 cases (c, d) as well as the PD_Base and PI_ALL cases (e, f). Differences significant at the 90% level according to a Student's t test are depicted by points.

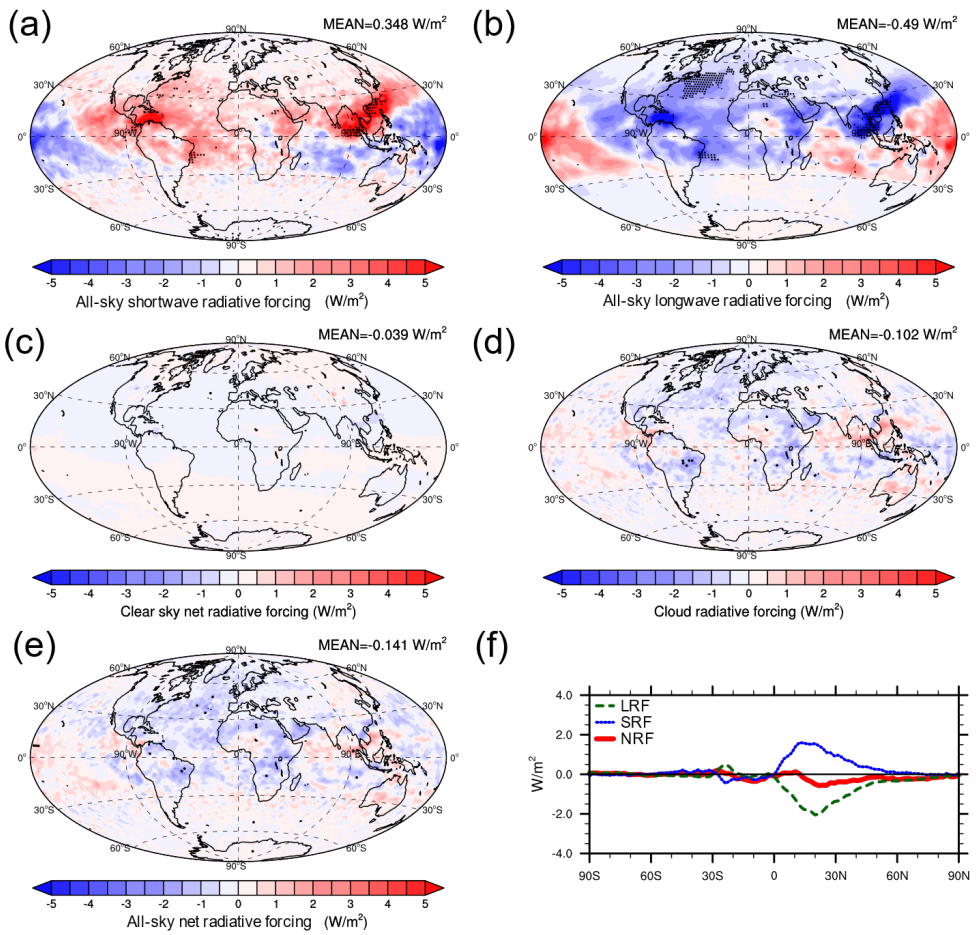

Figure 7. Annual mean plots of all-sky shortwave radiative forcing (a), all-sky longwave radiative forcing (b), clear sky net radiative forcing (c), cloud radiative forcing (d) and all-sky net radiative forcing (e) as well as all-sky longwave radiative forcing (f, LRF, green dashed line), all-sky shortwave radiative forcing (f, SRF, blue dotted line) and all-sky net radiative forcing (f, NRF, red solid line) versus latitude for the difference between the PD_Base and PI_cSoot cases. Differences significant at the 90% level according to a Student's t test are depicted by points.

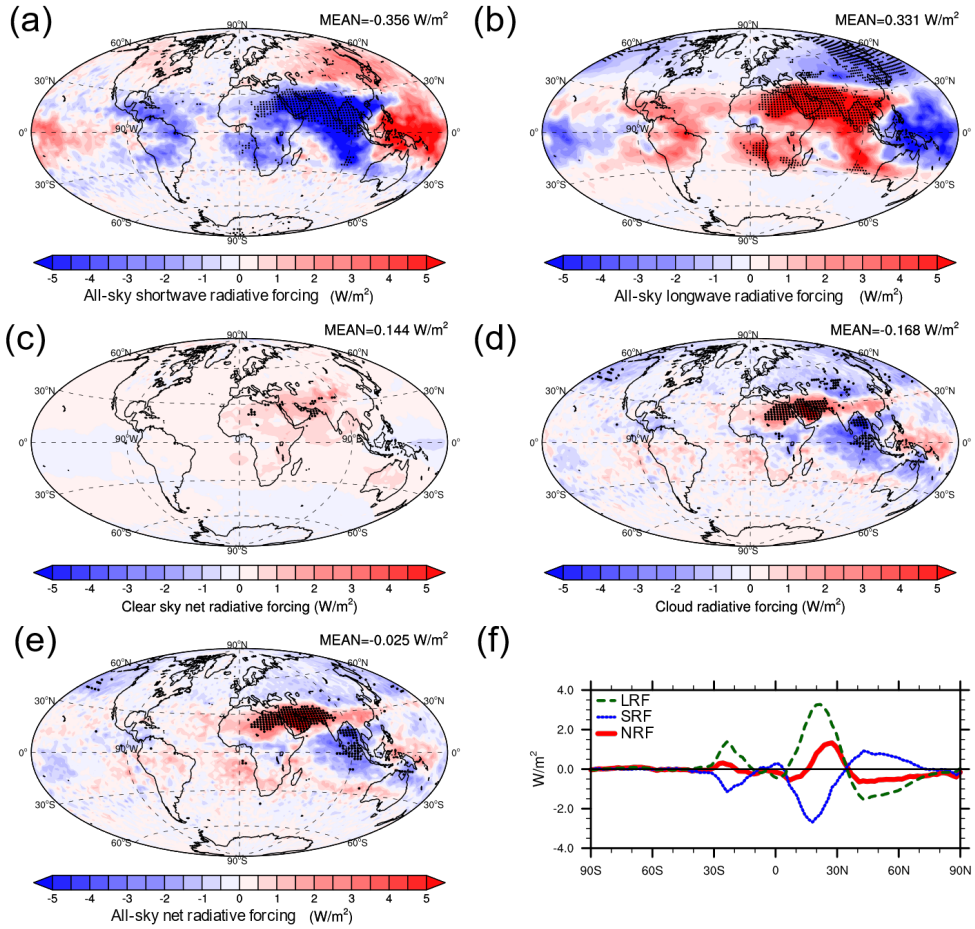

1212

1213 Figure 8. As in Figure 7 but for the difference between the PD_Base and PI_SO4

1214 cases. Differences significant at the 90% level according to a Student's t test are

1215 depicted by points.

1216

1217

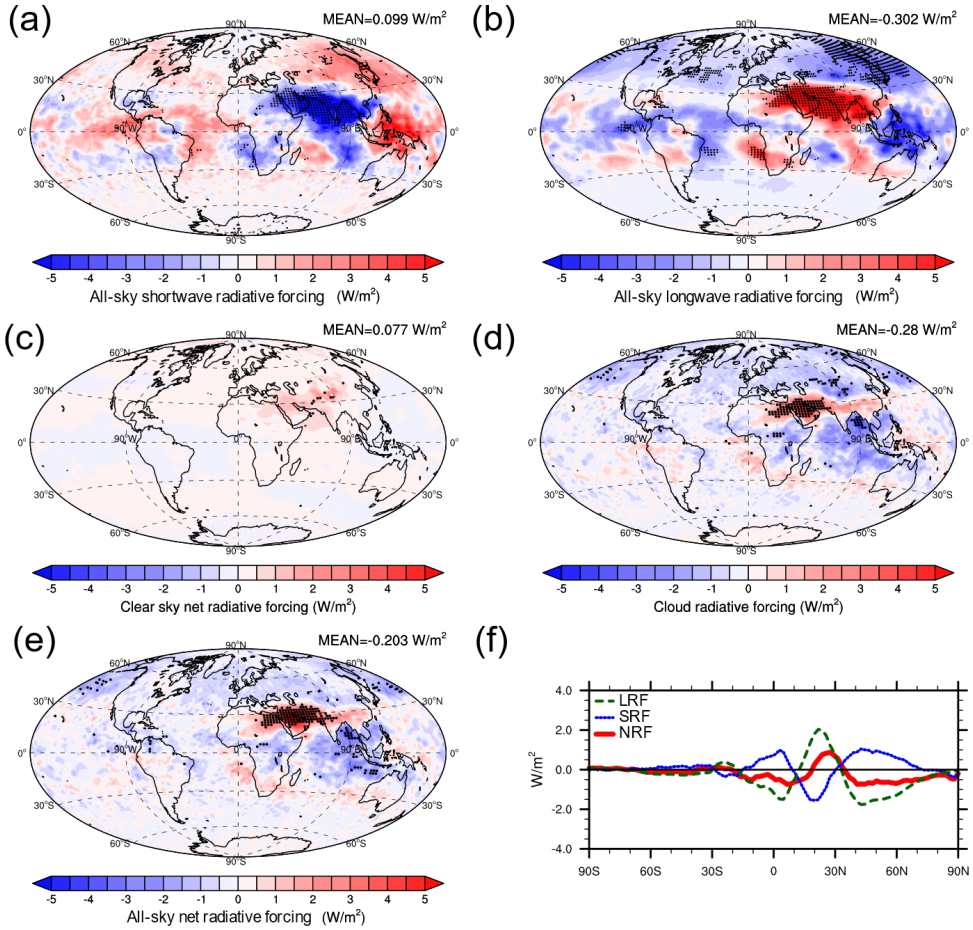

Figure 9. As in Figure 7 but for the difference between the PD_Base and PI_ALL cases. Differences significant at the 90% level according to a Student's t test are depicted by points.

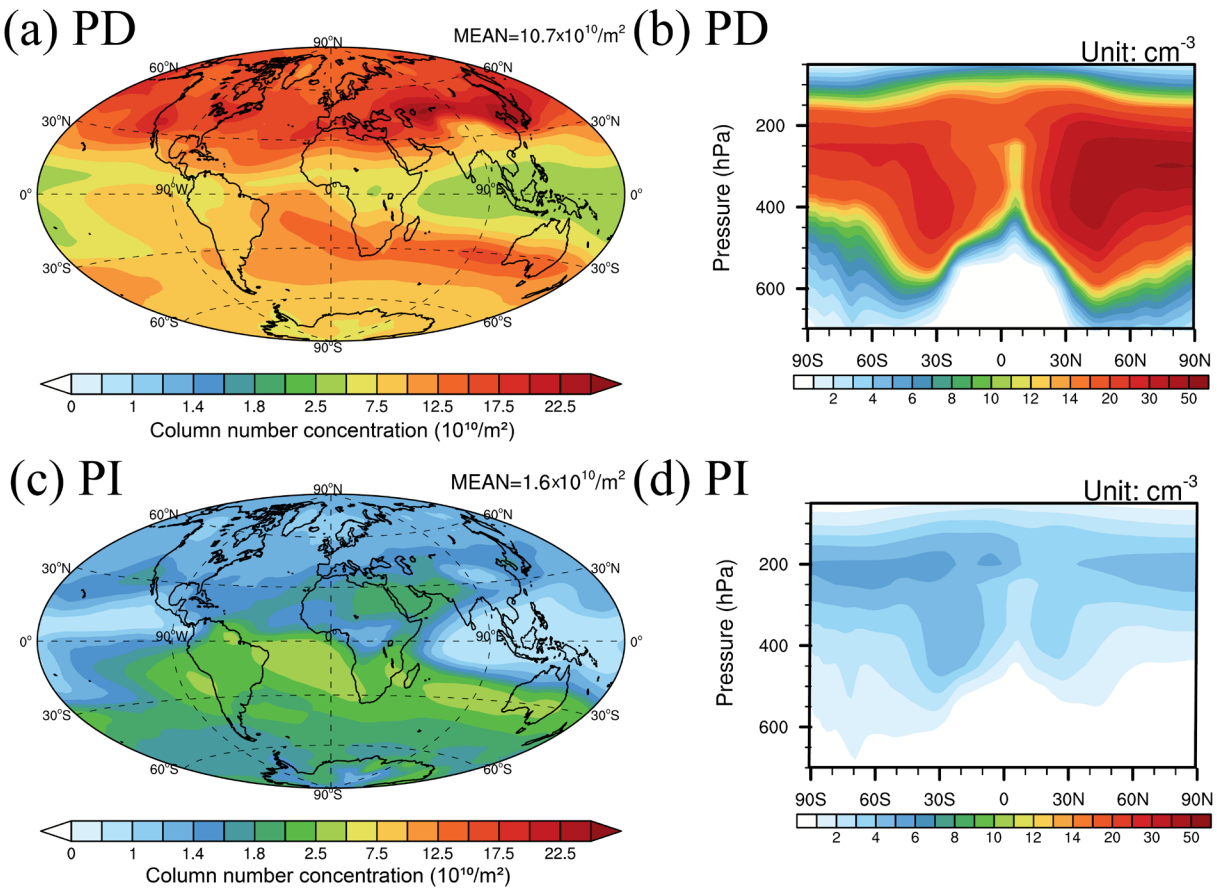

1225

1226 Figure 10. The vertically integrated number of INP (a, c) and zonal average plots

1227 of INP (b, d) from SOA in the PD_SOA (a, b) and PI_SOA (c, d) cases.

1228

1229

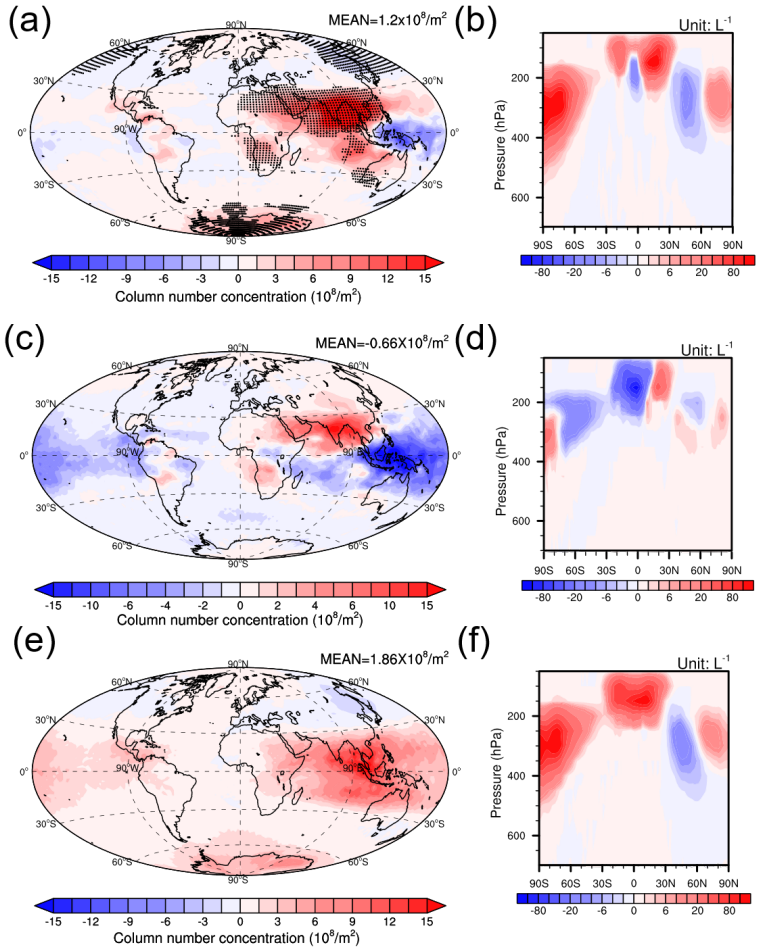

1230

1231 Figure 11. The annual average change in column number concentration (a, c, e)
1232 and zonal average number concentration (b, d, f) of total ice (a, b), ice from
1233 homogeneous nucleation (c, d) and ice from heterogeneous nucleation (e, f) for the
1234 difference between the PD_SOA and PI_SOA cases. Differences significant at the
1235 90% level according to a Student's t test are depicted by points.

1236

1237

1238

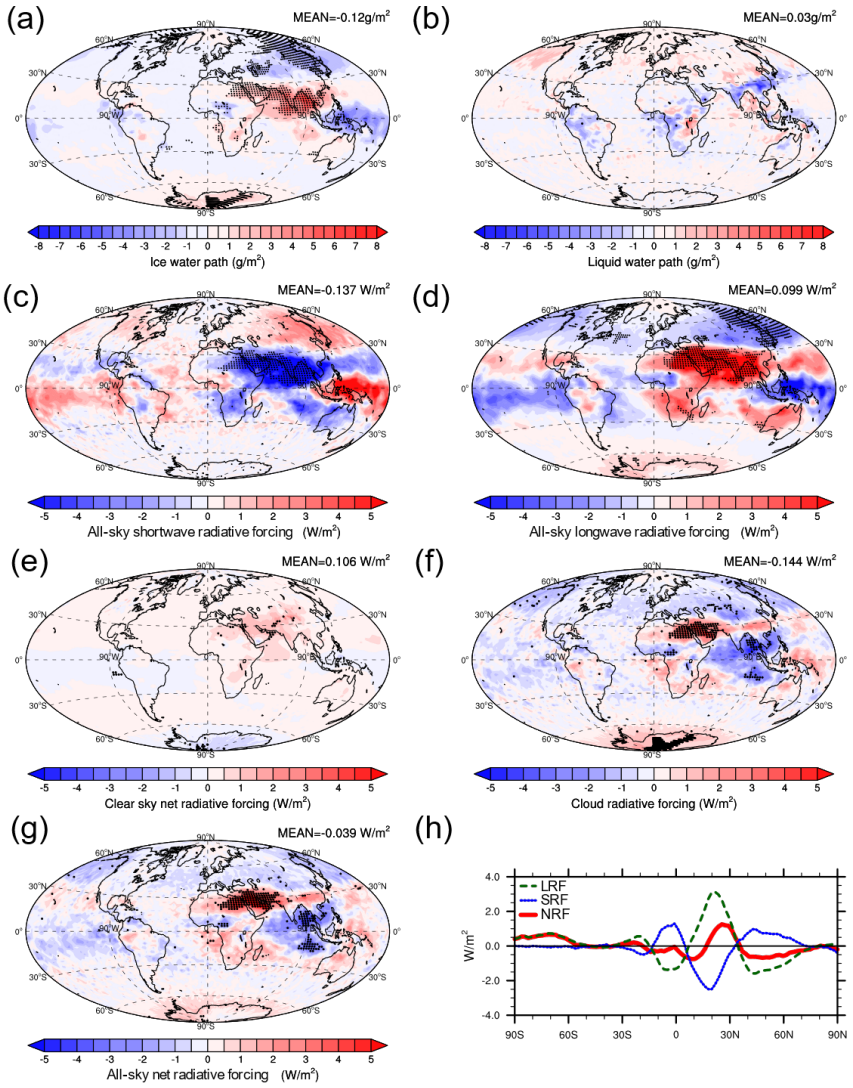

1239

1240 Figure 12. Annual mean plots of the changes in ice water path (a), liquid water
1241 path (b), all-sky shortwave radiative forcing (c), all-sky longwave radiative forcing
1242 (d), clear sky net radiative forcing (e), cloud radiative forcing (f) and all-sky net
1243 radiative forcing (g) as well as longwave radiative forcing (h, LRF, green dashed
1244 line), shortwave radiative forcing (h, SRF, blue dotted line) and all-sky net
1245 radiative forcing (h, NRF, red solid line) versus latitude for the difference between
1246 the PD_SOA and PI_SOA cases. Differences significant at the 90% level
1247 according to a Student's t test are depicted by points.

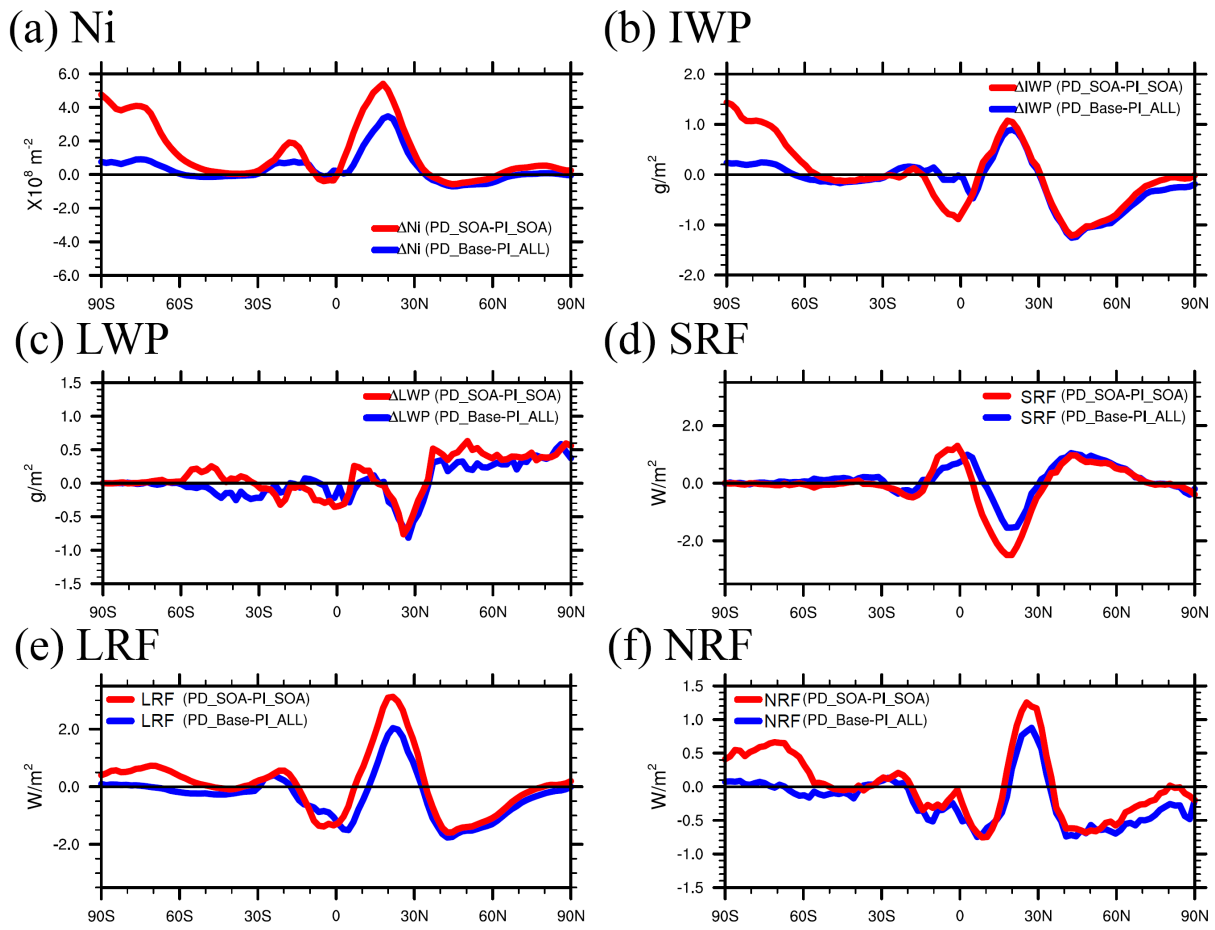

Figure 13. Change in vertically integrated ice number concentration (a), ice water path (b), liquid water path (c) as well as shortwave radiative forcing (d), longwave radiative foricng (e) and all-sky net radiative forcing (f) for the difference between the PD_SOA and PI_SOA cases (red line) as well as PD_Base and PI_ALL cases (blue line).